The Bingham Canyon Porphyry Cu-Mo-Au Deposit.
III. Zoned Copper-Gold Ore Deposition by Magmatic Vapor Expansion °

Marianne R. Landtwing,[1,*] Caroline Furrer,[1,**] Patrick B. Redmond,[2,‡] Thomas Pettke,[1,‡‡]
Marcel Guillong,[1,§] and Christoph A. Heinrich[3,†]

[1]*ETH Zurich, Department of Earth Sciences, Clausiusstrasse 25, 8092 Zurich, Switzerland*

[2]*Department of Geological and Environmental Sciences, Stanford University, Stanford, California 94305*

[3]*ETH Zurich, Department of Earth Sciences, Clausiusstrasse 25, 8092 Zurich, Switzerland, and
Faculty of Mathematics and Natural Sciences, University of Zurich*

Abstract

Fluid inclusion microthermometry and laser-ablation ICPMS microanalysis are combined with geological and textural observations to reconstruct the spatial and temporal evolution of magmatic fluids that formed the subvolcanic porphyry Cu-Au(-Mo) ore deposit at Bingham Canyon, Utah. The Bingham Canyon orebody is exposed over ~1.6 km vertically and has the shape of an inverted cup with distinct metal zoning.

Fluid inclusions in the barren but highly veined and potassically altered deep center of the system have intermediate density (~ 0.6 g cm^{-3}) and a salinity of ~7 wt percent NaCl equiv. They have subequal concentrations of Na, K, Fe, and Cu and contain minor CO_2. The intermediate-density fluids were trapped as a single phase, mostly at >500°C and >800 bars. The Au-Cu–rich center near the top of the orebody contains low-density vapor inclusions (~ 0.2 g cm^{-3}) coexisting with brine inclusions containing ~45 wt percent NaCl equiv. The vertical transition of different inclusion types indicates phase separation of the single-phase input fluid upon volume expansion associated with a pressure drop to 200 ± 100 bars. Mass-balance calculation based on all analyzed inclusion components indicates that the mass of the vapor phase exceeded that of the brine by ~9/1. The vapor contained Cu as its dominant cation (~1.5 wt %) and contributed about 95 percent of the total amount of copper transported to the base of the orebody. Bornite, chalcopyrite, and native gold were precipitated in a narrow temperature interval from 430° to 350°C, into secondary pore space created by local redissolution of vein quartz as a result of retrograde quartz solubility in the vapor-dominated fluid system.

Intermediate-density fluid inclusions in the deepest parts of the peripheral copper ore zone have identical density and composition, including similar gold contents, as those in the deep center. Microthermometry and statistical estimation of phase proportions in the inclusions show that the vapor in the peripheral Cu-rich but Au-poor ore zone remained denser, and the separating brine was less saline (~36 wt % NaCl equiv), compared to vapor and brine in the central Au-Cu ore zone. This indicates that the peripheral fluids experienced a lower degree of phase separation, due to slightly higher fluid pressure at equivalent temperature, compared to more strongly expanding fluids in the center of the system.

The systematic zoning of Au/Cu within the ore shell, despite compositionally similar input fluids, is interpreted to have resulted from slightly different pressure-temperature-density evolution paths of magmatic fluids. Copper was selectively precipitated in the peripheral ore zone, in contrast to complete coprecipitation of Au and Cu in the central upflow zone of the vapor plume. The formation of particularly rich Cu-Au ore in the center of the upward-expanding fluid plume is consistent with published experimental data, showing that the solubility of metals in hydrous vapor decreases sharply with falling pressure, due to destabilization of the hydration shell around metal complexes in expanding vapor. This interpretation supports the classic vapor plume model for porphyry copper ore formation but additionally emphasizes the role of sulfur-bearing complexes as a key chemical control on magmatic-hydrothermal metal transport and the deposition of Cu and Au in porphyry ores. Our interpretation of selective Cu ± Au precipitation as a function of vapor density can explain the more general observation that most gold-rich porphyry copper deposits are formed in shallow subvolcanic environments, whereas deeper seated porphyry Cu-(Mo) deposits are generally gold poor.

Introduction

Interpretations of porphyry-style ore formation over the last decades have become increasingly differentiated and quantitative, integrating the role of magmatic fluids exsolved from plutons underlying the mineralized stocks (e.g., Henley and McNabb, 1978) with the convection of external fluids driven by the thermal energy of magmatic intrusions (Taylor, 1974; Cathles, 1977), as reviewed by Hedenquist and Lowenstern (1994), Seedorff et al. (2005), and Sillitoe (2010). Early studies of fluid inclusions in porphyry copper deposits recognized two locally coexisting fluid phases, a high-salinity brine and a low-salinity vapor (Roedder,

*Present address: University of Teacher Education Central Switzerland (PHZ Luzern), Museggstrasse, Lucerne, Switzerland.
**Present address: Burstwiesenstrasse 53, 8606 Greifensee, Switzerland.
‡Teck Resources Limited, 550 Burrard Street, Vancouver, BC Canada V6C 0B3.
‡‡Present address: University of Bern, Baltzerstrasse, Bern, Switzerland.
§Present address: University of Tasmania, CODES, Private Bag 79, Hobart, Australia 7001.
† Corresponding author: e-mail, heinrich@erdw.ethz.ch
°A digital supplement to this paper is available at <http://www.geoscienceworld.org/> or, for subscribers, on the SEG website.

Acronyms Used in this Paper

BP = biotite prophyry
EDM = early dark micaceous
LP = latite porphyry
QLP = quartz latite porphyry
QMP = quartz monzonite porphyry

1971, 1992; Denis et al., 1980). Magmatic brine inclusions contain high ore metal concentrations, based on observations of chalcopyrite daughter crystals (e.g., Roedder, 1971; Nash, 1976; Denis et al., 1980), and experimental data indicated that chloride complexing allows transfer of copper from hydrous magmas to saline magmatic fluids (Candela and Holland, 1986; Candela and Piccoli, 1995). These observations led to the interpretation that chloride in saline magmatic fluids was the key ingredient in the formation of porphyry copper deposits (Lindgren, 1905; Dilles, 1987; Cline and Bodnar, 1991). Other studies suggested that the low-salinity magmatic vapor phase is the main fluid driving porphyry-style ore formation (Henley and McNabb, 1978; Giggenbach, 1992), consistent with early evidence indicating high Cu contents in low-salinity vapor inclusions (Etminan, 1977; Eastoe, 1978; Sawkins and Scherkenbach, 1981; Lowenstern et al., 1991).

Analytical studies of fluid inclusions from porphyry-style ore deposits and miarolitic cavities in barren and mineralized intrusions have quantified ore metal concentrations in a wide range of magmatic-hydrothermal fluids, showing that both phases can carry high concentrations of ore metals and sulfur (Audétat et al., 2008). Some of the highest copper and gold concentrations are recorded by low-salinity fluids of vaporlike density (Heinrich et al., 1992, 1999; Damman et al., 1996; Audétat et al., 1998; Ulrich et al., 1999; Baker et al., 2004; Klemm et al., 2007). These observations have spurred a new wave of experimental and conceptual studies, which demonstrate that hydrous magmatic vapor can transport high concentrations of ore metals (e.g., Williams et al., 1995; Archibald et al., 2002; Williams-Jones et al., 2002; Williams-Jones and Heinrich, 2005; Pokrovski et al., 2005, 2008; Simon et al., 2007; Nagaseki and Hayashi, 2008; Zezin et al., 2008).

This paper investigates the evolution of hydrothermal fluids of variable density and salinity in the Bingham Canyon Cu-Mo-Au deposit (Fig. 1), based on detailed microanalytical study of fluid inclusions. Bingham Canyon is an exceptionally large and rich deposit but exhibits geologic features that are typical for many other porphyry-style ore deposits. This includes a prominent metal zonation centered on an intrusive stock (see Gruen et al., 2010; Redmond and Einaudi, 2010). The ore shell has the shape of an inverted cup and is well exposed in the large open-pit mine and by deep diamond drill holes that have reached the base of the zoned orebody and its barren core, more than a kilometer below the center of the deposit (Fig. 2). This vertical exposure provides an opportunity to reconstruct the fluid evolution, both temporally in the evolving magmatic-hydrothermal system, as well as spatially from the deep region of fluid ascent to the region of zoned ore mineral precipitation. Fluid inclusions at Bingham Canyon are large and well preserved, suitable for pioneering technical and analytical studies (Roedder, 1971; Anderson et al., 1989; Irwin and Roedder, 1995; Bodnar, 1995; Kendrick et al., 2001a, b; Vanko et al., 2001; Redmond et al., 2004; Landtwing et al., 2005; Guillong et al., 2008). This fluid inclusion study builds on two companion papers documenting the intrusive history and paragenesis (Redmond and Einaudi, 2010) and the significance of intrusion and vein geometry, indicating that the structure of the ore shell resulted from radial extension above a broad high-pressure fluid source (Gruen et al., 2010). Detailed observations for this series of papers are

documented in five research theses at Stanford University and ETH Zurich by Inan (2002), Redmond (2002), Landtwing (2004), Furrer (2006), and Gruen (2007).

Mine-Scale Geology

The Bingham Canyon deposit is hosted by the Bingham stock, a polyphase subvolcanic intrusion of broadly monzonitic composition emplaced into Paleozoic quartzites, semipelitic siltstones, and impure carbonate rocks (Fig. 1). The sedimentary rocks were folded and thrusted during several phases of Mesozoic orogeny, prior to porphyry intrusion and hydrothermal mineralization in the late Eocene. Later block faulting by Basin-and-Range extension during the Oligocene to Pliocene led to 10° to 30° tilting and exposure of the deposit in the Oquirrh Mountains, west of Salt Lake City. This tilting preserved the southeastern flank of a former stratovolcano of comagmatic (broadly latitic) lavas and volcaniclastic rocks (Deino and Keith, 1997; Waite et al., 1997). Geologic relationships allowed an approximate reconstruction of the paleotopography at the time of volcanism and magmatic-hydrothermal mineralization, indicating ~2 km of rock overburden above the pre-mine top of the deposit (Deino and Keith, 1997).

The Bingham stock (Fig. 1) has a surface extent of ~3 × 3 km and comprises at least five intrusive phases (Redmond and Einaudi, 2010), starting with the premineralization equigranular monzonite and several nonmineralizing dikes that intruded it. The quartz monzonite porphyry (QMP) is a medium- to coarse-grained elongate stock, measuring about 1.5 × 0.4 km in plan, which intruded the more mafic equigranular monzonite along its northwest contact. The QMP was the focus of greatest intensity of veining, pervasive potassic alteration, and high-grade Cu-Au mineralization, which extended into the adjacent equigranular monzonite and (to a lesser extent) into the sedimentary wall rocks (Fig. 2). Thin (generally <50 m; Fig. 1) but more laterally extensive dikes of latite porphyry (LP) intruded later along the same axis as the QMP (Fig. 1). Although the LP dikes locally have a lower vein density and lower grade mineralization (Redmond and Einaudi, 2010), they have undergone pervasive biotite alteration of the groundmass and mafic phenocrysts. At the mine scale, Cu-Au distribution in the LP follows the same concentric pattern as that in the QMP, and the mineralized veinlets are indistinguishable except by truncations seen at some intrusive contacts. A fourth group of thin dikes include dark brown biotite porphyry (BP) of lamprophyric texture and composition and quartz latite porphyry (QLP), which intruded all earlier porphyries (mostly <20 m thickness). Both of the dike types were cut by minor stockwork veinlets with restricted biotite alteration.

The sequence of vein formation was independently recorded in numerous observation points throughout the deposit, based on intersection and overprinting relationships between veins, intrusive contacts, and different alteration types (Redmond et al., 2001; Redmond, 2002; Landtwing, 2004; Redmond and Einaudi, 2010; Gruen et al., 2010; Fig. 3). Wispy biotite veinlets and early dark micaceous (EDM) veins were the first, volumetrically minor, veins that formed after each of the mineralized intrusions. The EDM veins are marked by 1- to 2-cm-wide alteration halos, which locally have a thin (<3 mm) centerline of quartz. This quartz may have been deposited after reopening during the subsequent stockwork vein stage,
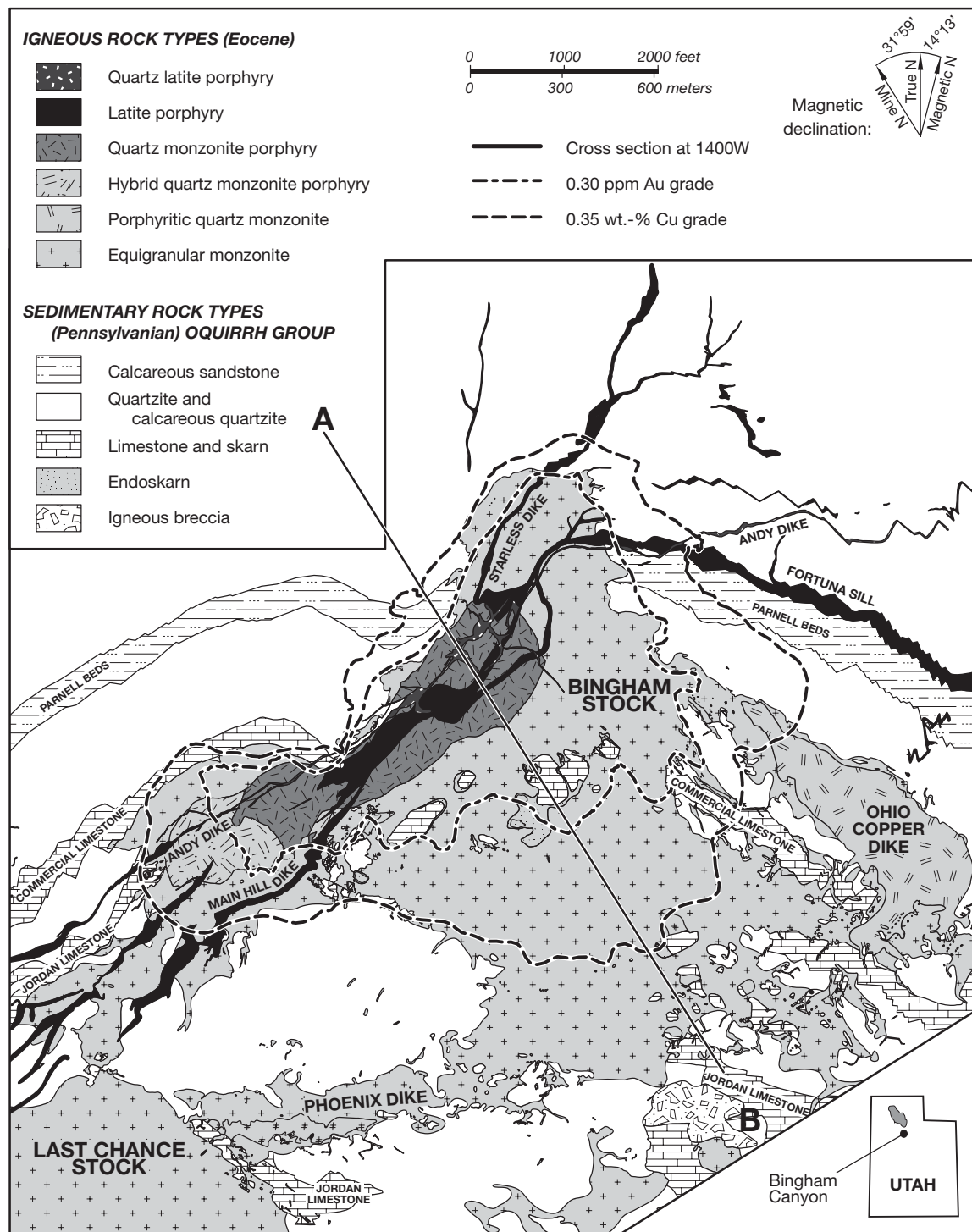
FIG. 1. Mine-scale map based on Kennecott Utah Copper, showing major lithologic units and ore-grade contours of >0.35 percent Cu and >0.3 percent Au before the pit surface intersected the barren core (mapping stage of 1998; compare with Gruen et al., 2010, fig. 2). Line A-B shows trace of cross section of Figures 3 and 7.

because the EDM veins formed at quartz-undersaturated conditions, as indicated by the typical alteration assemblage of sericite + biotite + K-feldspar ± andalusite ± corundum ± Cu-Fe sulfides. Quartz stockwork veins comprise a complex set of crosscutting veinlets. They are dominated by quartz infill and are surrounded by variably pervasive biotite-K-feldspar

alteration. Truncations by intrusive contacts demonstrate that quartz stockwork veins formed after solidification of each of the three mineralized intrusions (QMP, LP, and QLP) but with decreasing abundance and intensity of associated potassic alteration halos. The quartz stockwork veins (Fig. 3A, B) are typically 0.5 to 2 cm thick and have variable appearances,
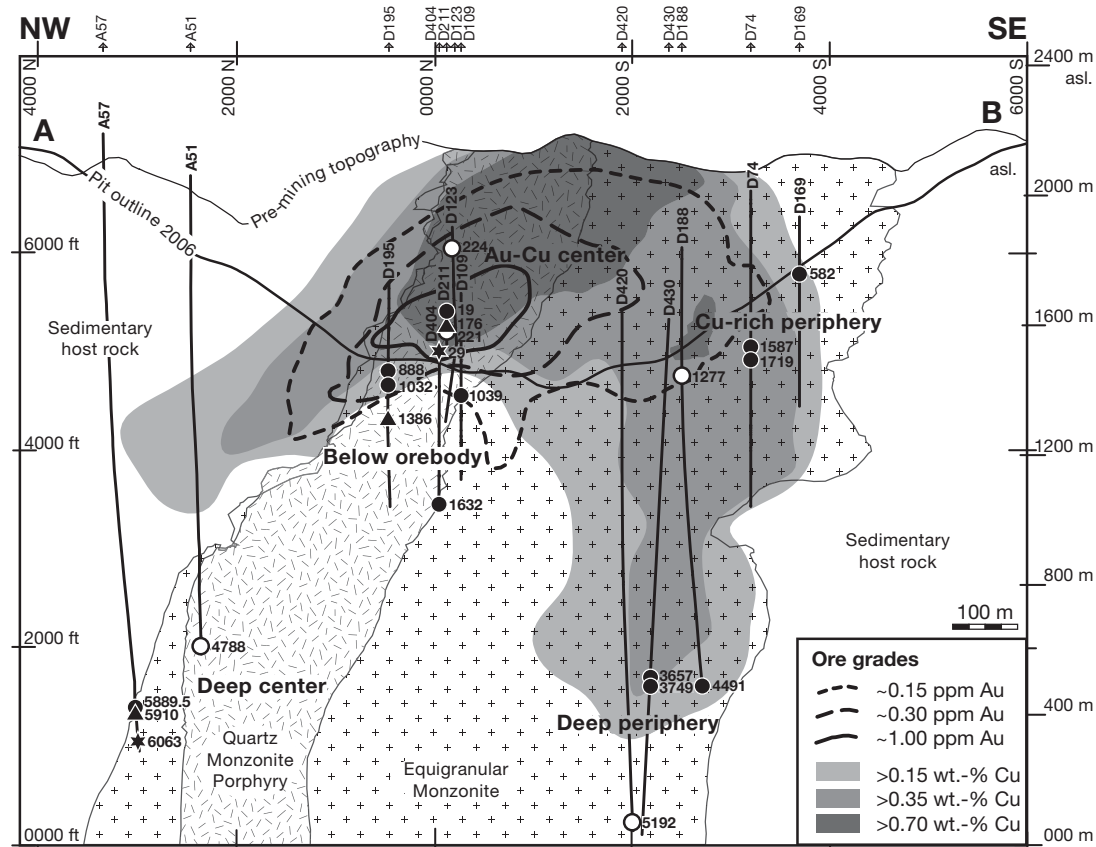
FIG. 2. Northwest-southeast cross section –1400E of the mine grid, perpendicular to the elongate QMP intrusion on which the zoned Cu-Au mineralization is centered. Note highest Cu-Au grade in the top of inverted cup-shaped orebody, and the Cu-rich but Au-poor limbs extending downward at the periphery of the system. Mo contours (not shown) largely follow Cu contours but tend to be slightly displaced downward toward the barren center below the Au-Cu–rich orebody (Gruen et al., 2010). Grid in mine coordinates (ft). Sampling regions and sample points in drill holes and surface projection (Table 1) are indicated, black dots denoting quartz stockwork veins analyzed by LA-ICPMS, black triangles are quartz-molybdenite veins analyzed by LA-ICPMS, and white dots are quartz stockwork veins studied by fluid inclusion statistics. Two additional stockwork vein samples measured by microthermometry by Redmond (2002) are marked with black stars. Sample D411-2646.5 (off section) and surface samples 4990-2050, 5090-1510, 5090-1525, and 5190-1600 (collected near the collar of drill hole 211) are not included in this Figure.

from early irregular-walled glassy or granular quartz veins to more straight-walled veins with symmetric columnar quartz infill. They generally have no open spaces, and only some show a well-defined centerline. In contrast to the multiple phases of stockwork veins, quartz-molybdenite veins postdate all intrusions including QLP (Fig. 3B). The veins are 1 to 5 cm wide, typically have at least one meter of lateral extent, and consist of blocky to euhedral quartz and coarse flakes of molybdenite that grew from straight walls into still partially open space. Quartz-pyrite veins with sericitic alteration are straight-sided to anastomosing and occur as vertically extensive swarms of thin (< 1 cm) fractures filled by pyrite, minor quartz ± calcite ± chalcopyrite ± bornite. The quartz-pyrite veins with sericitic alteration are surrounded by halos of a few centimeters to several meters extent, in which all feldspars and most mafic minerals have been altered to sericite and/or illite, pyrite, and in some cases chlorite (Fig. 3C).

Methods

The fluid inclusion study reported here is based on approximately 500 samples, which were collected during systematic

mapping and core logging to document the time relationships of major vein types and the contained minerals. Figure 2 and Table 1 define five sampling regions with regard to simplified geology (Redmond and Einaudi, 2010) and large-scale Cu and Au grade distribution (Gruen et al., 2010). More than half of the samples from the open-pit surface and from drill cores were taken in the vicinity of section –1400E, i.e., the main cross section discussed in the two preceding papers. The focus of this paper is on the quartz stockwork veins, which are intimately linked to the zoned Cu and Au mineralization, and with potassic alteration extending into the deep barren center of the ore system. Most samples are hosted by QMP and EM away from contacts with later intrusions. This sampling strategy avoids postentrapment modification of inclusions by reheating due to local intrusions but introduces the uncertainty that the fluids cannot be uniquely associated with the main mineralizing QMP phase, although this is statistically most likely in light of the decreasing vein density associated with later and volumetrically minor dikes. We have not selectively sampled the volumetrically minor quartz stockwork veins cutting the later porphyry dikes (Redmond and Einaudi, 2010),
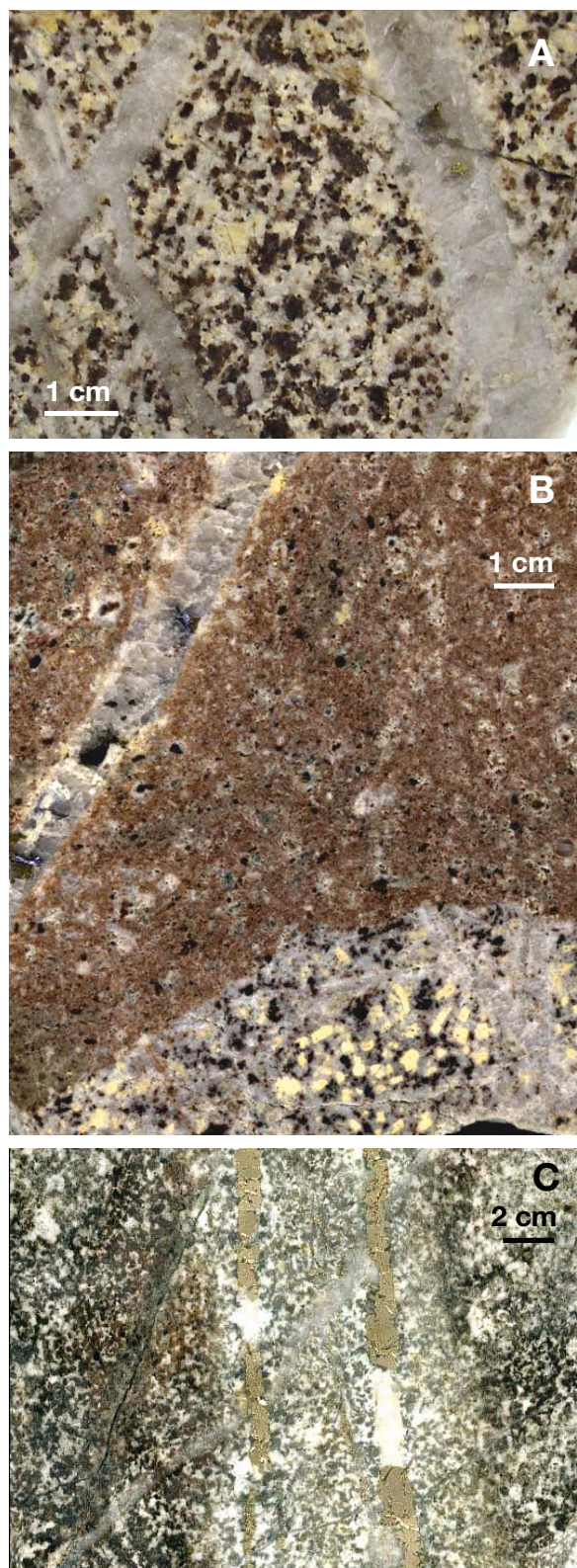
FIG. 3. Photographs of slabs of the three main vein types studied by fluid inclusion analysis. (A). Quartz stockwork veins in biotite-altered equigranular monzonite. (B). Quartz-molybdenite vein cutting biotite-altered LP, which intruded QMP that had previously been Cu-Au mineralized by the main stage of stockwork veining (lower part of photo). (C). Quartz-pyrite veins with sericitic alteration cutting and overprinting earlier stockwork veins, as the last event of magmatic-hydrothermal mineralization.

which is a limitation of the present study. However, a few quartz-molybdenite veins were sampled preferably where there was direct evidence that the vein has cut by a late BP or QLP dike.

Several hundred vein samples were prepared as quickplates for inspection of inclusion type and quality, i.e., showing the largest and best preserved inclusions in clearly identifiable assemblages (spatially associated groups of coeval inclusions with similar petrographic appearance and constant phase proportions at room temperature; Goldstein and Reynolds, 1994). A subset of 80 sections was polished and studied by conventional reflected and transmitted light microscopy. Cathodoluminescence imaging on a scanning electron microscope (SEM-CL) of the majority of these samples revealed at least two quartz generations in each vein, which could be correlated with the history of fluid inclusion entrapment in selected quartz-Cu-Fe sulfide veins (Redmond et al., 2004; Landwing et al., 2005). As detailed in Table 1, a selection of 27 doubly polished sections were studied by a combination of cathodoluminescence petrography, microthermometry, laser ablation inductively coupled plasma mass spectrometry (LA-ICPMS) and/or statistical evaluation of phase proportions at room temperature. All microthermometric and LA-ICPMS data were collected from petrographically defined inclusion assemblages rather than individual inclusions to allow calculation of averages and standard deviations (1σ) whenever several measurements of a particular property or analytical concentration ratio was obtained from individual inclusions in the assemblage. All analytical data points in this paper refer to such assemblages, as tabulated in the digital supplement. This approach ensures that analytical errors or uncertainties due to imperfect trapping or inclusion preservation (variability within one assemblage) can be distinguished from true geologic variation in paleofluid properties (differences between assemblages; Goldstein and Reynolds, 1994; Heinrich et al., 2003). Relating such variations to geologic time, however, is generally not possible because the majority of identifiable and measureable fluid inclusion assemblages are secondary or pseudosecondary in origin. Unambiguously primary inclusions do occur as faint brownish-colored crystal growth zones in many veins, but they are invariably too small for quantitative analysis (<2 μm) or even for phase type identification.

Mapping of fluid inclusion characteristics identified a systematic variation in predominant inclusion types with regard to depth (Redmond et al., 2004) and also indicated that phase proportions in the brine and vapor inclusions varied systematically from the Au-Cu–rich center of the orebody to the Au-poor peripheral Cu ore zone of the system (Fig. 2). Five of the samples described in Table 1 were studied with a previously untested statistical approach; two from the Cu-rich periphery of the orebody and three samples from the center of the system in and below the high-grade Au-Cu orebody. In each petrographic section, two- and three-phase inclusions were counted along random straight lines as indicated in Figure 4. Inclusions with a minimum dimension of 20 μm and a depth from the surface of 10 ± 5 μm (depth of focus) intersected by a reference line in the X-Y stage of the microscope were counted until exactly 60 two-phase inclusions (liquid + vapor ± small opaque crystal) or 60 three-phase inclusions (liquid + vapor + halite ± other daughter crystals) were

TABLE 1. Summary Description of Samples, Veins, and Fluid Inclusions

Sampling sites			Samples: Vein, wall-rock, and alteration mineralogy; methods and data source					
Location	Main lithologic units	Alteration	Sample no.	Vein type	Vein minerals additional to qtz	Vein selvage	Vein width (mm)	Wall rock
Deep center	QMP, (QLP, EM, sedimentary rock)	–Potassic –Weak phyllic overprint (argillization of plag phenocrysts)	A51-4788	Molybdenite veinlet reopening a barren quartz stockwork vein		Kspar	8	QMP
			A57-5889.5	Quartz stockwork vein (white qtz)		qtz, Kspar	9	QMP
			A57-5910	Quartz molybdenite vein (fine-grained, banded with undulating, irregular borders, anastomosing)	moly (distinct zones), cc, zeo, Kspar		8	QLP
			A57-6063	Quartz stockwork vein (barren)			8	QMP
Center below orebody	QMP, EM, (LP, QLP)	–Potassic –Propyllitic overprint of EM –Weak phyllic overprint (argillization of plag phenocrysts)	D109-1039	Quartz stockwork vein (barren, parallel-walled, banded, blocky qtz)	Kspar, cc (in vugs), minor cpy	White Kspar	6	QMP
			D195-1386(A)	Quartz-molybdenite vein (gray, clear qtz, 12 vol % idiomorphic moly flakes in distinct zones)	moly (crystals up to 5 mm)		10	LP
			D404-1632	Two crosscutting quartz stockwork veins (fine-grained, weakly zoned; blocky, coarse-grained)		Kspar	4/2-7	QMP
Au-Cu center, lower part	QMP, LP, QLP	–Potassic –Weak phyllic overprint (argillization of plag phenocysts)	D195-888	Early dark micaceous vein (irregular, anastomosing centerline, 15 mm brown-green alteration selvage)	Kspar	qtz, Kspar, mica, bn, cov, cpy	2-3	QMP
			D195-1032	Quartz stockwork veins (two qtz gen.: earlier milky phenocrysts, reopening with clear, gray qtz)	Minor py		10	QMP
			D211-221	Quartz stockwork vein (vuggy, clear qtz)	cpy, bn		8	QMP
Au-Cu center, upper part	QMP, LP, QLP	–Potassic –Weak phyllic overprint (argillization of plag phenocysts)	D123-224	Quartz stockwork vein (clear to gray qtz)	cpy		10	QMP
			D211-19	Quartz stockwork vein (parallel-walled, clear qtz)	cpy, bn		12	QMP
			D211-176	Quartz-molybdenite vein (sparry, crosscutting gray quartz stockwork vein with cpy, bn, Kspar)	moly		10	QMP
			D404-29	Quartz stockwork vein (clear qtz)	bn, dig, cpy		9	QMP
			4990-2050	Quartz-chalcopyrite-molybdenite vein (sparry, gray, clear)	moly		10	QMP
			5090-1510	Quartz stockwork vein (clear to gray qtz)	bn, dig, cpy		8	QMP

Observations, Ordered by Sampling Regions shown in Figure 3

							Fluid inclusions: types, description and data extent			
Alteration/matrix mineralization	Measure-ments	Thesis	# CL gen.	Sulfide with # CL gen.	Fluid inclusion types	Fluid inclusion description (dc = daughter crystal)	# assem. MT ID/B/V/A	# single FI MT ID/B/V/A	# assem. LA ID/B/V/A	# single FI LA ID/B/V/A
Potassic, weak phyllic op./barren	SA/CL	F/R	—	—	ID,(B,V)	ID: small inclusions, irregularly to regularly shaped, ±1 opaque dc (cpy)	—	—	—	—
Potassic, weak phyllic op./barren	LA,MT,CL	L	1	—	ID,(B,V)	ID, V: up to 30 μm, regular to negative crystal shaped/ID: two gen./B, V: postdating ID/B: regularly shaped, <15 μm, 1 opaque dc	ID18/B4/V4	ID234/B68/V19	ID17/B8/V6	ID64/B19/V15
Potassic/barren	LA,MT,CL	L	1	—	ID,(B,V)	ID, B, V: <15 μm, irregular to regular shaped; B, V: postdating ID; ID: ±1 opaque dc ID: containing CO_2	ID7/B2	ID59/B6	ID5/B3	ID18/B3
Potassic/barren	MT,CL	R	—	—	ID		ID1/B1	ID7/B1	—	—
Potassic, weak phyllic op./barren	LA,MT,CL	L	2	—	B,V,(A)	B, V: regularly to negative crystal shaped, up to 30 μm; B: 1 opaque dc, 1-2 transparent dc	B13	B307	B13/V4	B44/V4
Potassic/barren	LA,MT,CL	L	3	3	B,V,(A)	B, V: irregularly to regularly shaped, up to 25 μm; B: 2 opaque dc (cpy, moly), 2-3 transparent dc	B19	B366	B19/A1	B40/A1
Potassic/barren	LA,MT/CL	L/R	1/2	2	B,V,(A)	B, V: 1 opaque daughter crystal, up to 30 μm	B10	B124	B6	B13
Potassic/disseminated cpy, bn	LA,MT,CL	L	1	—	B,V,(A)	B, V: regularly to negative crystal shaped, <15 μm	B5	B59	B3	B8
Potassic, weak phyllic op./minor disseminated cpy, bn	LA,MT/CL	F/L	2	(2)	B,V,(A)	B: up to 40 μm, 1 opaque dc (cpy), 2-3 transparent dc; V: up to 40 μm, 1 opaque dc (cpy)	B3/V3	B21/V20	B4/V4	B20/V25
Potassic, weak phyllic op./disseminated cpy, bn	SA	F			B,V,(A)	B, V: up to 45 μm, irregularly to regularly shaped; B: 1-2 opaque dc (cpy, hem), 2-4 transparent dc	—	—	—	—
Potassic/minor disseminated cpy	SA/CL	F/L	2	2	B,V,(A)	B, V: up to 50 μm; B: 1-2 opaque dc (cpy, hem), 2-4 transparent dc	—	—	—	—
Potassic/disseminated cpy, bn	LA,MT,CL	L	2	2	B,V,(A)	B, V: two gen., second gen. associated with second gen. of qtz; B: ±1-2 opaque dc, 1-3 transparent dc	B96/V16/A4	B926/V97/A23	B56/V32/A1	B156/V79/A3
Potassic/minor disseminated cpy, bn	LA,MT,CL	L	1	1	B,V,(A)	B, V: multiple gen., irregularly to regularly shaped, up to 15 μm	B2/V5/A2	B26/V37/A8	B3/V1	B5/V4
Potassic/disseminated cpy, bn	MT,CL	R	2	2	B,V,(A)	B, V: up to 50 μm, two gen., second gen. associated with copper deposition and second gen. of qtz	B1	B9	—	—
Potassic/minor disseminated cpy, bn	LA,MT	L	—	—	B,V,(A)	B, V: multiple gen., irregularly to regularly shaped, up to 15 μm; B: 1-2 opaque dc (cpy, hem), 2-3 transparent dc	B3/V2/A2	B44/V12/A8	B2/V1	B9/V5
Potassic/disseminated cpy, bn	MT,CL	R	—	—	B,V,(A)	B, V: irregularly to regularly shaped	B1	B13	—	—

TABLE 1.

| Sampling sites | | | Samples: Vein, wall-rock, and alteration mineralogy; methods and data source | | | | | |
Location	Main lithologic units	Alteration	Sample no.	Vein type	Vein minerals additional to qtz	Vein selvage	Vein width (mm)	Wall rock
Au-Cu center, upper part	QMP, LP, QLP	–Potassic –Weak phyllic overprint (argillization of plag phenocysts)	5090-1525	Quartz stockwork vein (two gen. of qtz)	cpy, bn, dig		9	QMP
			5190-1600	Quartz stockwork vein (gray, clear, sheeted)	cpy, bn		10	LP
Cu-rich periphery	EM	–Potassic –Propyllitic overprint –Phyllic overprint along cm-dm wide fractures	D74-1719	Quartz stockwork vein (zoned, reopening of clear qtz, abundant sulfides)	py, minor cpy and cc		15	EM
			D74-1587	Quartz stockwork vein (~15 vol % cpy, three stages of qtz, gray (1st, 70 vol %) and clear (2nd, 3rd) qtz)	cpy as fracture fillings and crystals, py		9-11	EM
			D169-582	Quartz stockwork vein	cpy and cc		7	EM
			D188-1277	Quartz stockwork vein (milky to clear qtz, sulfides in center of vein and as fracture fillings)	py, cpy as fracture fillings		7	EM
			D411-2646.5	Quartz-sericite-pyrite vein (py-qtz-bn-cpy, minor qtz, 8 mm to dm wide sericitic selvage)	py, cpy , bn, cov, enargite, rutile	sericite	5	EM
Deep periphery	EM	–Potassic –Propyllitic overprint	D188-4491	Quartz stockwork vein (milky to clear qtz, with abundant sulfides)	py, minor cpy		15	EM
			D420-5192	Quartz stockwork vein (clear to milky qtz with abundant sulfides)	py, minor cpy	bio	5	EM
			D430-3657	Two crosscutting quartz stockwork veins (clear, gray qtz)	py, cpy minor cc		3/4	EM
			D430-3749	Reopened quartz stockwork vein (blocky qtz)	cpy, cc		5	EM

Notes: Sample locations: the first digits of each drill core sample indicate the drill core number, whereas the second number gives the depths from the collar in feet (e.g., sample D211-19: drill core D211 taken 19-ft depths below the collar); surface samples 4990-2050, 5090-1510, 5090-1525, and 5190-1600 are collected near the collar of drill hole D211 (Fig. 3); sample D411-2646.5 is out of section originating from drill core collared at 325.6 E/2597.55 N at 5832.2-ft elevation

Abbreviations: General: assem. = assemblages; dc = daughter crystal; gen. = generation/generations; op. = overprint; FI = fluid inclusions

Measurements: SA = statistical analysis of distribution of inclusion types and phase proportions (cf. Fig. 4); LA = LA-ICPMS; MT = microthermometry; CL = SEM-cathodoluminescence

reached. This always occurred first for the two-phase inclusions, providing a measure of the lower abundance of brine inclusions seen in all samples. Each selected inclusion was photographed digitally through a 40× objective. For each inclusion, bubble, liquid, and solids were hand-traced in Adobe Photoshop®, and areas were pixel-counted to give a measure of area proportions of the three phases. These were plotted in frequency diagrams and converted to approximate volume proportions assuming a spherical vapor bubble and a halite cube inside a spherical inclusion. Even though imprecise for individual inclusions, the averaged area measurements yield a statistically unbiased and independent estimate of the average density of the two-phase

(Cont.)

							# assem. MT ID/B/V/A	# single FI MT ID/B/V/A	# assem. LA ID/B/V/A	# single FI LA ID/B/V/A
				Sulfide	Fluid					
Alteration/matrix mineralization	Measure-ments	Thesis	# CL gen.	with # CL gen.	inclusion types	Fluid inclusion description (dc = daughter crystal)				
Potassic/dissem-inated cpy, bn	MT	R	—	—	B,V,(A)	B, V: two gen., second gen. associated with second gen. of qtz	B1	B14	—	—
Potassic/dissem-inated cpy, bn	LA,MT	L	—	—	B,V,(A)	B, V: up to 15 μm, some inclusions trapped in apatite; B: ±1 opaque dc (cpy, hem), 1-2 transparent dc	B1/V2	B10/V13	B2/V1	B8/V3
Potassic, propylitic op./disseminated cpy, bn	LA,MT	F	—	—	B,V,(A)	B, V: up to 50 μm; B: 1-2 transparent dc, 1 opaque dc	B2/V8	B13/V36	B2/V4	B11/V21
Potassic/dissem-inated cpy	LA,MT,CL	L	3	2 and 3	B,V,A	B, V: irregularly to regularly shaped, <20 μm, clusters in 1st gen. of qtz, trails in 2nd and 3rd but same chemical composition; B: ±1 opaque dc	B9/V3	B279/V11	B13	B37
Strong potassic/ disseminated cpy	LA,MT	F	—	—	ID,B,V	ID: predominating, up to 45 μm; minor V, B, up to 45 μm	ID5	ID33	ID6	ID49
Potassic/dissem-inated py, cpy	SA/CL	F/L	2	2	B,V,ID	B, V: predominating, up to 30 μm; B: 1 opaque dc, 1-2 transparent dc; minor ID, very small.	—	—	—	—
Potassic, phyllic op./minor dissem-inated cpy, bn	LA,MT,CL	L	3	1 py 2 cpy	A	A: CO$_2$ bearing, <10 μm, irregularly or regularly shaped, some inclusions 1 opaque dc	A19	A148	A5	A10
Weak potassic, weak propylitic op. disseminated py, cpy	LA,MT	F	—	—	ID,(B,V)	ID: predominating, up to 20 μm; 1 opaque dc (hem)	ID4/B1	ID23/B4	ID4/B1	ID30/B5
Potassic, propylitic op./abundant dissem-inated py, cpy	SA/CL	F/L	1	1	ID,(B,V)	ID: predominating, up to 30 μm; minor V, B	—	—	—	—
Strong potassic/ minor disseminated py, cpy	LA,MT	F	—	—	ID,(V)	ID: predominating, secondary, up to 25 μm; minor V, 5-10 μm	ID2	ID9	ID2	ID9
Potassic, weak propylitic op./ disseminated cpy	LA,MT	F	—	—	ID,(B,V)	ID: predominating, up to 20 μm, 1 opaque dc; minor V, B, small	ID8/B1	ID37/B5	ID8	ID40

Fluid inclusion types: ID = intermediate density; V = vapor; B = brine; A = aequeous liquid

Minerals: cc = calcite; Kspar = K-feldspar; plag = plagioclase; qtz = quartz; zeo = zeolite; bn = bornite; cov = covellite; cpy = chalcopyrite; dig = digen-ite; hem = hematite; moly = molybdenite; py = pyrite

Thesis: F = Furrer; (2006); L = Landtwing (2004); R = Redmond (2002)

Full data for of 236 LA-ICPMS fluid inclusion assemblages (with 758 individual fluid inclusions measured) and for the distribution of fluid inclusion types and phase proportions statistic samples are available as a digital supplement at <http://www.geoscienceworld.org/>

inclusions (ignoring CO$_2$ and minor salt species) and of the average total salinity of brines, assuming 26.5 percent NaCl in the liquid phase (saturation concentration at 25°C) with den-sity 1.2 g cm^{-3} and a halite density of 2.16 g cm^{-3}.

In 18 samples, a total of 236 different inclusion assemblages were measured with a combination of microthermometry and LA-ICPMS analysis. This corresponds to 758 individual inclusions with 1 to 15 inclusions per assemblage; four addi-tional samples were studied by microthermometry only (see right-hand columns in Table 1 for overview information and digital supplement for all assemblage data). Low-temperature phase transitions and halite dissolution temperatures up to
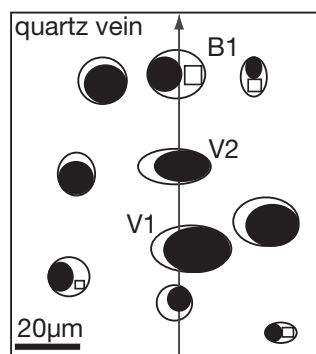
FIG. 4. Methodology for statistical analysis of phase proportions of vapor, liquid, and salt crystals in fluid inclusions of selected stockwork vein samples. For unbiased selection, every inclusion cut by an arbitrary straight driving track (arrow) exceeding 20 μm in size was counted for frequency estimation of inclusion types and photographed for subsequent area measurement.

~300°C were usually measured first, whereas final homogenization experiments were done at the end on a few inclusions in each assemblage saved from destructive elemental analysis. LA-ICPMS microanalysis on the prototype instrument at ETH Zurich allows online petrographic control and optimized quartz ablation (Günther et al., 1997, 1998; Pettke et al., 2000). Note that LA-ICPMS measures ratios of element concentrations only. Determining absolute concentrations requires a combination of this element ratio analysis with a concentration constraint from microthermometry, usually expressed as apparent salinity in wt percent NaCl equiv, and an assumption to estimate the true Na concentration by combination with the LA-ICPMS analysis (see Heinrich et al., 2003, for calculation methods and discussion of uncertainties). Abundant K, Fe, and Cu show that the Bingham Canyon fluids strongly deviate from the binary NaCl-H_2O system. Moreover, apparent salinities of two-phase inclusions were difficult to quantify due to the presence of significant CO_2. Therefore, LA-ICPMS data plots and genetic interpretations are primarily based on the directly measured element ratios relative to Na (digital supplement). To obtain the representative fluid compositions shown in Tables 2 and 3, we combined mass-balance constraints with the measurements from microthermometry and LA-ICPMS analyses, as explained in the Discussion section below. Limits of detection were calculated for each inclusion (Günther et al., 1998; Heinrich et al., 2003), which typically results in some values for trace components (notably Au) that are below the average of detected values in the inclusion assemblage. This implies a

tendency for overestimating the average concentration ratio in an assemblage due to the short signal duration (Pettke et al., 2000). There is no possibility to quantify and correct this potential error, but it does not affect the main conclusions from this study.

Vein Petrography and Fluid Inclusion Results

Quartz sulfide textures from SEM-CL

Quartz stockwork veins: Associated with Cu-Au mineralization these veins are generally massive and have a macroscopically glassy to granular appearance. Some contain a line of small pink K-feldspar crystals growing on the vein wall or inside the vein. Others contain a calcite-filled centerline but no macroscopic open spaces. In thin section and transmitted light, the quartz texture is mostly granular, but some brown growth bands consisting of submicroscopic fluid or melt inclusions demonstrate precipitation into open space. Most quartz grains are anhedral and interlocked. Cathodoluminescence (SEM-CL) imaging revealed a complex but consistent internal growth structure (Redmond et al., 2004; Landtwing et al., 2005; Fig. 5). Similar to observations from other porphyry deposits (Rusk and Reed, 2002; Klemm et al., 2007, 2008), the quartz stockwork veins at Bingham Canyon record two main stages of quartz crystallization (Fig. 5; Redmond et al., 2004). An early bright-luminescent quartz generation (Q1) constitutes the bulk of each quartz vein (>80 vol %). In deep barren stockwork veins, Q1 is homogeneously bright luminescent and fills most of the vein volume (Fig. 5A-C), whereas in the Cu ± Au mineralized ore zone it commonly shows complex oscillatory zoning, from bright to gray CL intensity (Fig. 5D-H). Intact Q1 grains were never observed to contain inclusions of Cu-Fe sulfides or gold. A second, dull- to nonluminescent quartz generation Q2 constitutes at most 20 vol percent of the veins. It occurs on cracks and grain boundaries that cut and overgrew Q1 in crystallographic continuity and commonly truncated earlier growth bands in Q1 (Fig 5D, G). Textures indicate that a process of microbrecciation and dissolution of Q1 occurred prior to recementation by Q2. Chalcopyrite and composite bornite-digenite grains invariably are in contact with and commonly surrounded by this dull-luminescent quartz Q2, which also extends along microcracks and grain boundaries into the potassically altered wall

FIG. 5. Characteristic textures in three vein types, as shown by SEM-CL (left), BSE images (center), and a small transmitted light micrograph for overview (right). Note that CL brightness is adjusted for optimal contrast in each composite map but not equivalent between the three samples shown. (A-C, sample A57-5889.5): Detail from three mutually intersecting parallel-walled quartz stockwork veinlets from the deep center in barren but pervasively biotite-altered QMP, with granular gray to milky macroscopic appearance; ~5 percent open space appears white in the BSE image (B) due to Ce-rich polishing powder but may have originally been filled with calcite; CL image (A) shows poorly zoned anhedral quartz grains with CL bright to CL gray luminescence in all three veinlets. (D, H, sample D211-19): Quartz stockwork vein from the Au-Cu center, with a thin K-feldspar selvage in pervasive biotite-altered QMP; vein interior shown in images contains bornite, digenite, and chalcopyrite; cathodoluminescence image reveals complex quartz textures, including euhedral growth zoning in early quartz generation Q1, followed by fracturing and dissolution surfaces; fracture-filling later generation of quartz Q2 overgrows earlier zoning and shown faint CL dull growth bands (not visible due to low contrast); sulfides are entirely enclosed in this later quartz Q2. (I-K, sample D411-2646.5): Pyrite-quartz-bornite-chalcopyrite vein with centimeter-wide sericitic selvages, cutting earlier stockwork veins with potassic alteration in the Au-Cu center; CL petrography reveals three quartz generations: 1st generation quartz is CL gray to CL dark luminescent and exhibits multiple irregular zoning; later quartz with no or only weak internal structures, with relatively bright (2nd generation) or dark (3rd generation) luminescence; mapping of sulfide inclusions reveals that pyrite is restricted to the first generation of quartz, 2nd generation quartz contains bornite and chalcopyrite inclusions but no inclusions of pyrite; 3rd quartz generation is generally free of any sulfide inclusions.
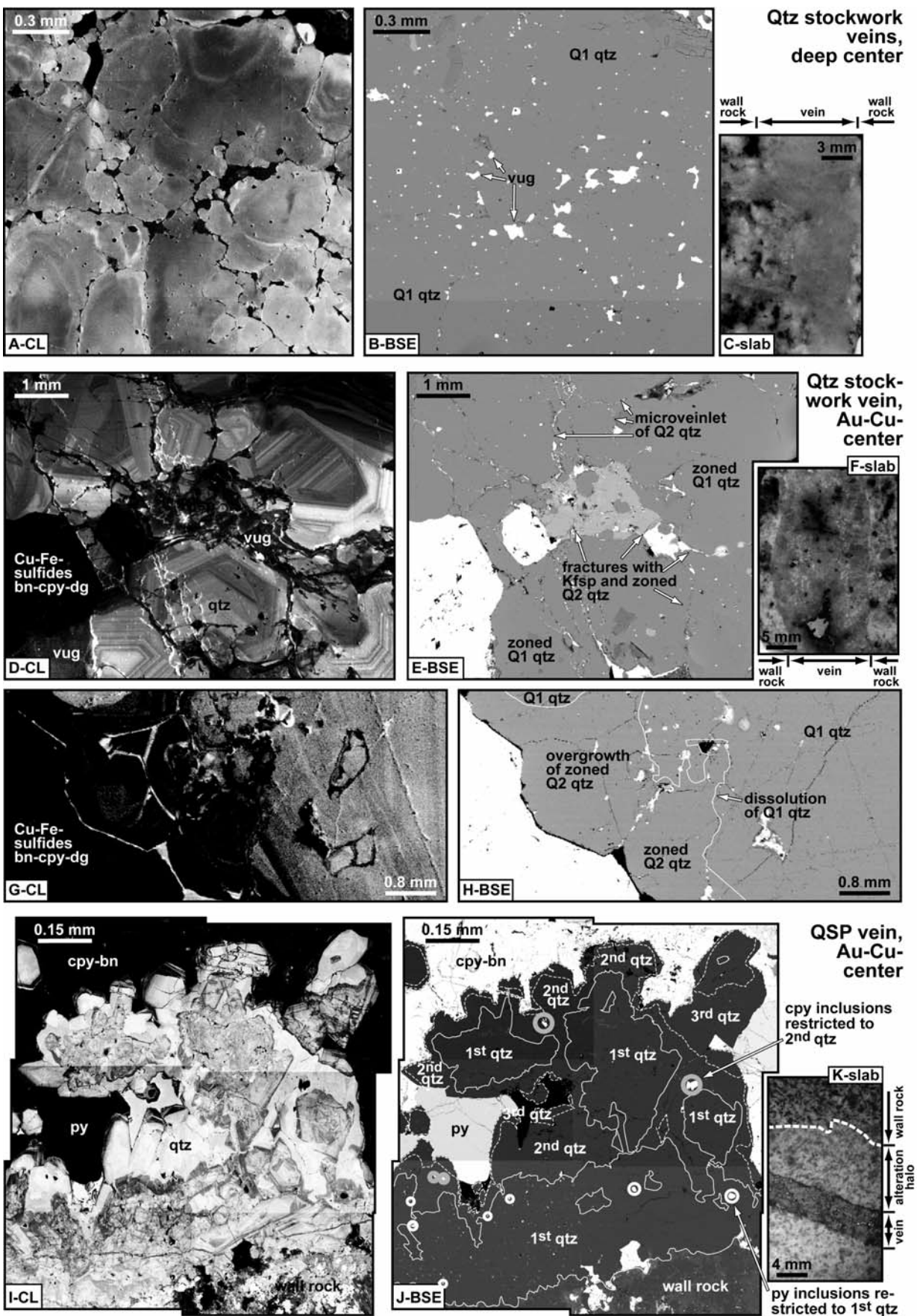
rock. Cu-Fe sulfides thus precipitated during or after Q1 dissolution and before or during recementation of veins and wall rocks by Q2. Bright, luminescent Q1 quartz contains significantly higher concentrations of trace elements (up to a few hundred ppm Ti, Al; tens of ppm Na, K) compared with dull, luminescent Q2 quartz (Landtwing and Pettke, 2005). In contrast to many other porphyry copper deposits, anhydrite (or gypsum) is absent at Bingham Canyon, and hydrothermal magnetite is uncommon in the mine, except in some deep drill holes and in minor quantity associated with distal propylitic alteration of monzonite.

Quartz-molybdenite veins: These veins commonly contain open spaces lined by euhedral quartz crystals, which overgrow a more massive granular zone along the vein walls showing similar texture and internal growth structures as the stockwork veins. In contrast to the Cu-Fe sulfides, molybdenite commonly precipitated before or together with a later generation of bright-luminescent quartz: as symmetric lines of euhedral flakes growing immediately adjacent to the vein walls, as bands inside the granular quartz, or as free-standing blades overgrowing the euhedral vug crystals. Minor chalcopyrite (but never bornite) crystallized late in the molybdenite veins, mostly as euhedral crystals in the central vugs.

Quartz-pyrite veins with sericitic alteration: These veins typically contain only minor amounts of a last generation of quartz, which occurs as small euhedral crystals lining the vein walls. This quartz is generally dull or nonluminescent and was overgrown first by euhedral pyrite and finally by calcite filling the remaining spaces. Some veins with sericite alteration halos have complex transitional characteristics, as exemplified by sample D411-2646.5. Backscattered electron (BSE) and SEM-CL mapping of quartz generations and sulfide inclusions in this sample (Fig. 5I-K) indicates early CL dull quartz + pyrite (generally characteristic of simpler quartz-pyrite veins with sericitic alteration) overgrown by a more luminescent second quartz generation with chalcopyrite + bornite inclusions, followed by a third generation of CL dark quartz that lines former vugs filled with chalcopyrite + bornite + pyrite ± calcite.

Distribution of inclusion types and phase proportions

Inclusion types are classified according to phases seen at room temperature (Fig. 6). Two-phase inclusions are subdivided into intermediate-density inclusions (type ID; Fig. 6A) containing comparable proportions of liquid and bubble at room temperature, vapor inclusions (type V; Fig. 6B, D, F) containing a bubble that occupies the greater part of the inclusions, and aqueous liquid inclusions (type A; Fig 6H) containing mostly aqueous solution and a smaller vapor bubble. Many intermediate-density and vapor inclusions contain a small opaque daughter crystal of constant relative size. Most type A inclusions are free of true daughter crystals but some contain sericite grains that are interpreted to be the product of accidental entrapment from ajdacent, sericite-altered wall rocks. Brine inclusions (type B; Fig. 6C, E, G) always contain a vapor bubble, a saline aqueous liquid, and halite. Polyphase brine inclusions contain additional daughter crystals, such as sylvite, plus transparent or opaque crystals, most notably small red hematite flakes and triangular chalcopyrite.

The spatial distribution of inclusion types varies vertically and horizontally with reference to the regions defined in Figure 2. Small "thumbnail" symbols in Figure 7 show the qualitative distribution of intermediate density, vapor, and brine inclusions in quartz stockwork veins within the representative cross section –1400E (Redmond et al., 2004; Figs. 3, 7). Intermediate-density inclusions predominate in the deep center and the deep periphery below the peripheral Cu ore zones. Intermediate-density inclusions are by far the dominant inclusion type below ~800 m a.s.l. and occur together with brine and vapor inclusions in an intervening zone, up to an elevation of ~1,100 m but still below the Au-Cu–rich center of the orebody, where they give way to vapor and brine inclusions only. Throughout the Au-Cu–rich center and the upper parts of the Cu-rich periphery, vapor and brine inclusions predominate in close association with each other. Occasionally, vapor and brine inclusions were found to occur on single healed microcracks (boiling trails; Audétat et al., 1998; Heinrich et al., 1999), demonstrating that the two fluid types coexisted as immiscible vapor and hypersaline liquid at trapping conditions (see digital supplement). In the periphery of the system, intermediate-density inclusions extend upward to shallower depth, compared to the deep barren center of the system (e.g., sample D169-582). This is indicated by the upward-concave lines delimiting the small inclusion symbols in Figure 7 (cf. Redmond et al., 2004). Distribution boundaries of fluid inclusion types cross the downward-concave copper grade contours delimiting high-grade copper ore, which extends to greater depth toward the periphery of the system (Fig. 7).

Inclusion distribution in other vein types was studied less systematically. EDM veins commonly do not have much open-space filling quartz, except due to later reopening, and the contained brine and vapor inclusions are therefore of uncertain association. Quartz-molybdenite veins have essentially similar inclusions as the quartz stockwork veins associated with Cu ± Au mineralization. A molybdenite vein cutting a late QLP dike in the deep barren center contains intermediate-density inclusions, similar to the earlier formed barren stockwork veins in EM and QMP in the same region (Table 1). Aqueous (type A) fluid inclusions with moderate to small bubble size predominate in quartz-bearing pyrite veins associated with postore sericitic alteration (quartz-pyrite veins with sericitic selvages).

Phase proportions within two- and three-phase inclusions trapped in quartz stockwork veins were measured by area counting in five representative veins (Fig. 4). Five triangle insets in Figure 7 illustrate a systematic variation in the density of two-phase fluid inclusions and in the salinity of brines, confirming the qualitative observations from other samples (compare Fig. 6D, E with F, G). Liquid/vapor ratios in the two-phase inclusions, plotting along the upper right edge of each triangle, decrease with elevation along the center of the system. The trend corresponds to an approximate decrease in average density from 0.63 g cm^{-3} in intermediate-density fluids from the deep center, to 0.26 g cm^{-3} for vapor inclusions from below the orebody, to 0.19 g cm^{-3} in the Au-Cu center (using the highest available sample location from a historic core above the present mine surface). On the deep periphery
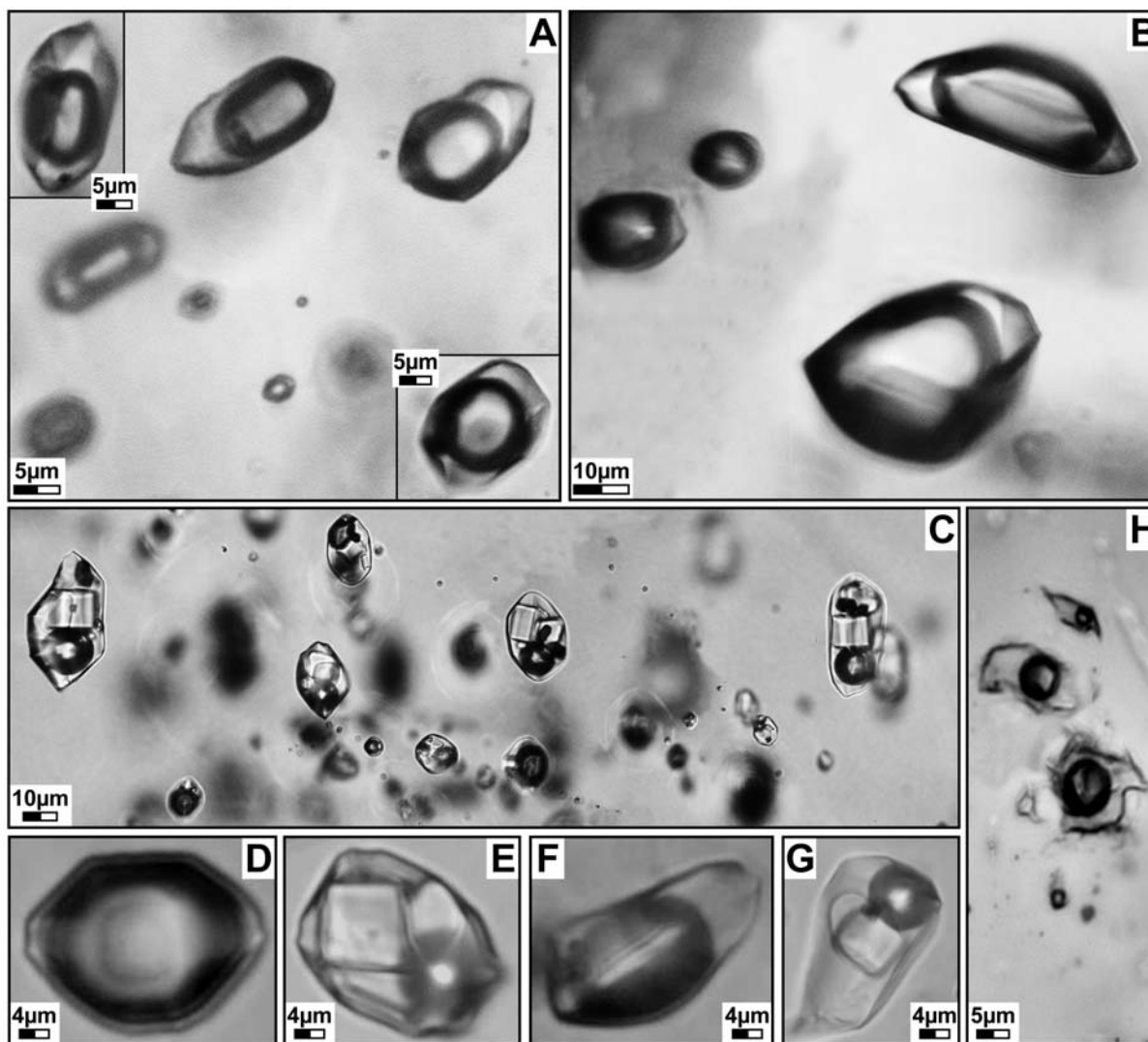
FIG. 6. Four main types of fluid inclusions measured at Bingham Canyon: Intermediate-density inclusions with similar proportions of liquid + vapor and a small opaque daughter crystal (A); vapor inclusions with similar appearance but significantly greater vapor bubble (B, D, F); brine inclusions with halite + liquid + vapor ± additional daughter crystals including sylvite, hematite, and other small transparent and opaque crystals (C, E, G); aqueous inclusions with predominantly liquid water and smaller vapor bubbles ranging from 20 to 40 vol percent (H). Bottom row of small photos D-G depict typical appearance of vapor and brine inclusions in the Au-Cu–rich center of the deposit (D, E: thin rim of liquid in vapor inclusions, high proportion of salts in brine inclusions) compared with those from the Cu-rich periphery (F, G: higher liquid/bubble ratio in both inclusion types, smaller salt crystal in brine inclusions). Sample numbers: (A) D420-4084; (B, H) D211-19; (C) 208-37; (D, E) D123-224; (F, G) D188-1277; (H) D411-2646.5.

(at the base of the Cu-rich part of the orebody), two-phase fluids are indistinguishable from those in the deep center, but they maintain a greater liquid fraction up to shallower depth. Phase volume estimates indicate a less pronounced decrease in average density from ~0.58 g cm^{-3} in intermediate-density fluids in the deep periphery, to a dense vapor or intermediate-density fluid with ~0.46 g cm^{-3} occurring with brine in the Cu-rich periphery near the outer margin of the orebody at the elevation of the present open pit. Brine inclusions are three times less frequent than two-phase inclusions in this sample.

The type B inclusions show an even more conspicuous difference between center and periphery (Fig. 6E vs. G). Brine inclusions in the center contain abundant and large salt crystals, which occupy about the same area in microscope view as the liquid phase (average h/l ~0.9/1 where h denotes halite + sylvite), whereas brines in the periphery have notably smaller halite crystals, usually no sylvite, and a significantly greater proportion of aqueous liquid (h/l ~0.3/1). Recalculating the area measurements into approximate volume fractions of salt crystal(s) and halite-saturated liquid indicates an average total salinity of 51 to 54 wt percent NaCl equiv in the Au-Cu center, increasing from the lower to the higher sample, compared to only 40 wt percent NaCl equiv in the Cu-rich periphery at similar elevation. The average bubble size in the type B inclusions, v/(v + l + h), is slightly higher in the Au-Cu center
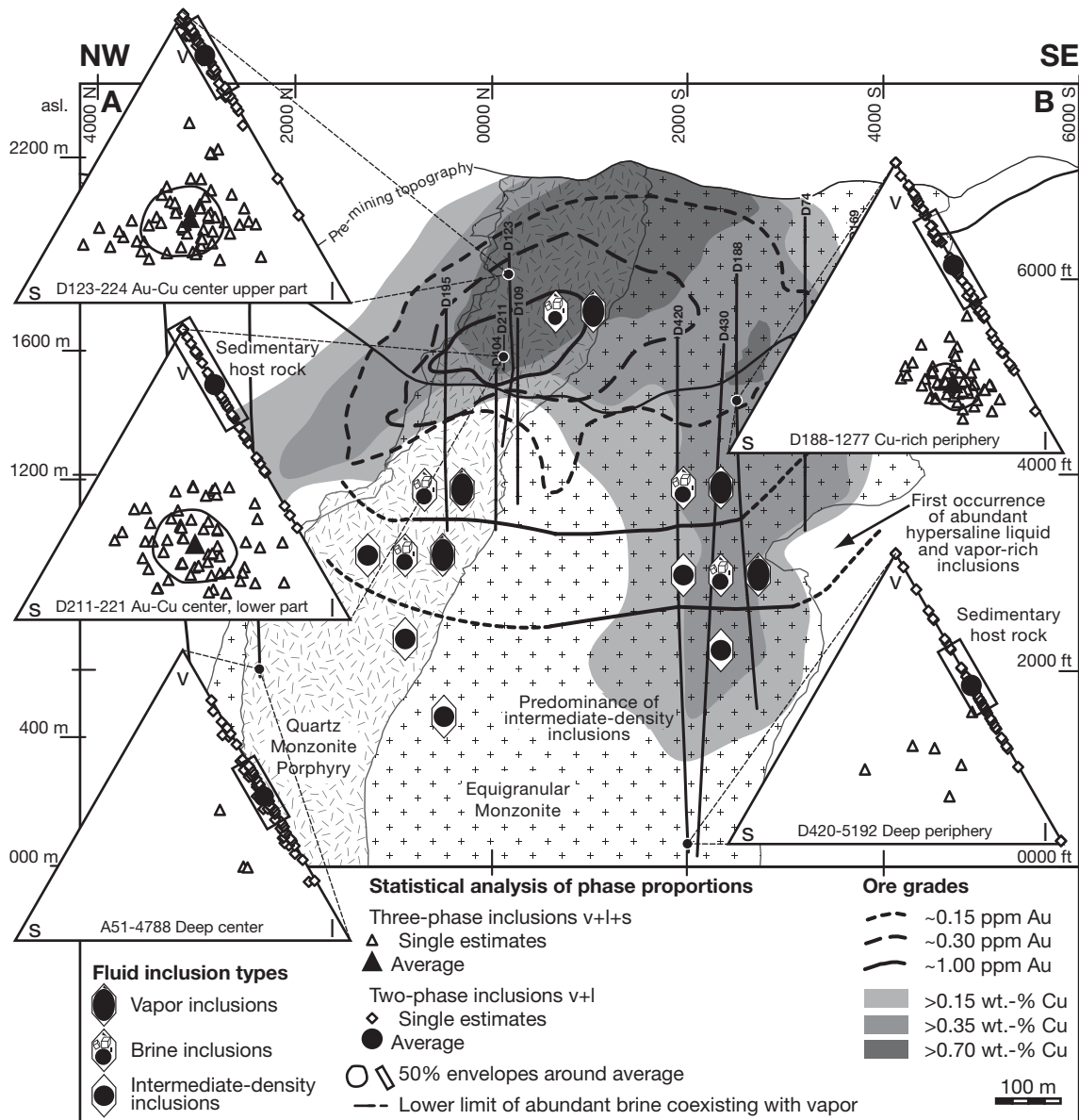
FIG. 7. Distribution of fluid inclusion types and liquid / vapor / halite phase proportions in barren and Cu ± Au mineralized quartz stockwork veins, plotted on the northwest-southeast geologic cross section of Figure 3. Distribution of dominant inclusion types is indicated by two thick lines and thumbnail symbols; phase proportions of vapor bubble (v), halite + other salt crystals (s), and aqueous liquid (l), measured by area percent, are plotted in triangular diagrams for five samples. Large black symbols and line contours in the triangular plots denote averages and 50 percentile envelopes of up to 60 inclusions of each type measured per sample.

(0.26 by area fraction) compared to the periphery at similar paleoelevation (0.21), in line with the density difference estimated for the vapor inclusions between center and periphery.

Microthermometric data

Microthermometric data were combined from several stages of investigation and are individually documented in the theses of Redmond (2002), Landtwing (2004), and Furrer (2006). Clearly definable petrographic assemblages and good consistency within most inclusion assemblages indicate good preservation of composition and bulk densities. No boiling trails with halite dissolution temperature significantly higher than vapor-bubble disappearance were observed at Bingham Canyon, which in other deposits is clear evidence for postentrapment modification of inclusions (e.g., Audétat and Günther 1999; Klemm et al., 2007, 2008).

Intermediate-density (type ID) inclusions show reasonably consistent phase transition temperatures within assemblages, but the measurements are difficult to interpret. Minor CO_2 is ubiquitous, as indicated by melting events close to $-56.6° ± 0.5°C$ and consistent clathrate melting between 1° and 8°C. This does not uniquely determine inclusion salinity, because the CO_2 content is too small to saturate a well-visible liquid CO_2 phase. Figure 8 (based on Diamond, 1992) summarizes
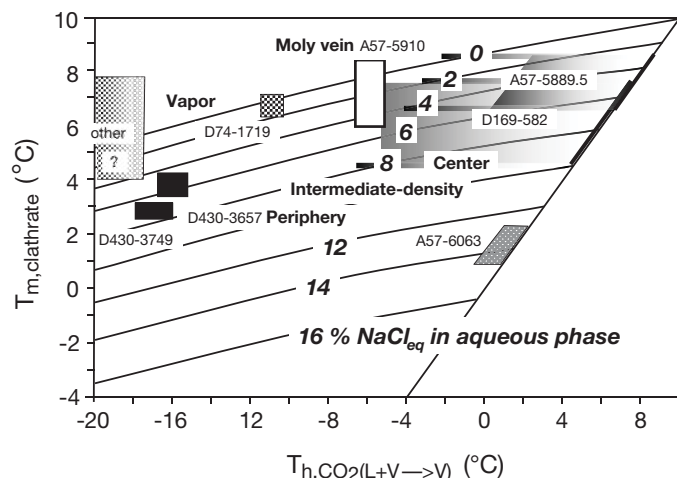
FIG. 8. Diagram based on figure 5 of Diamond (1992), showing isolines of fluid salinity as a function of the last melting of clathrate (T$_{m(clathrate)}$ vertical axis) against the temperature of homogenization of the CO$_2$ phase from L + V to V (T$_{h(CO_2)}$; dew-point homogenization of the carbonic phase). Limited constraints on salinities of intermediate-density (type ID) and vapor (V) inclusions at Bingham Canyon are plotted as boxes and discussed in the text.

the few measurements constraining the salinity of two-phase (L + V) inclusions of intermediate or vaporlike density, based on observations of CO$_2$ and clathrate melting. The clearest salinity measurements were obtained from two assemblages of intermediate-density inclusions in the Cu-rich periphery of the deposit, where the homogenization of the CO$_2$ phase and the last melting of clathrate were both unambiguously and reproducibly measured, indicating salinities of 5.8 ± 1.4 and 7.2

± 1 wt percent NaCl equiv (Furrer, 2006). Intermediate-density inclusions in one assemblage in the deep barren center of the deposit indicate a relatively high salinity of ~13 wt percent NaCl equiv based on a low temperature of last clathrate melting in the presence of liquid CO$_2$ (Redmond, 2002; sample A57-6063), but numerous other intermediate-density assemblages in the same region have higher clathrate melting (5°–8.5°C). Given the likelihood that liquid CO$_2$ was overlooked in these commonly small inclusions, this would indicate salinities below about 5 ± 2 wt percent NaCl equiv (Fig. 8). Intermediate-density inclusions beneath the central Au-Cu orebody homogenize by meniscus fading or by bubble expansion to the vapor phase at temperatures varying from ~365° to 429° ± 14°C (or even higher in sample A57-5889.5). Such homogenization behavior above 380°C is only possible if the inclusions contain significant salt as well as CO$_2$ (Gehrig, 1980). Intermediate-density inclusion in several samples from the deep base of the peripheral Cu zone (5.8–7.2 wt % NaCl equiv) homogenize to the liquid phase within a narrow range of 361° ± 4° to 384° ± 11°C (Furrer, 2006; Fig. 9). This indicates that the deep single-phase fluids in the periphery have slightly higher density but lower temperature (at similar depth and composition), compared with the single-phase fluids in the barren core below the center of the deposit.

The molybdenite-bearing vein cutting a late QLP dike in the deep center (sample A57-5910) contains intermediate-density inclusions homogenizing by meniscus fading or to the vapor at 390° ± 30°C. These inclusions contain liquid CO$_2$ and clathrate with measurable temperatures, constraining their salinity to 2.5 ± 2.5 wt percent NaCl equiv (Fig. 8).

Vapor inclusions (type V) are the predominant inclusion type in all stockwork veins of the Bingham Canyon orebody.
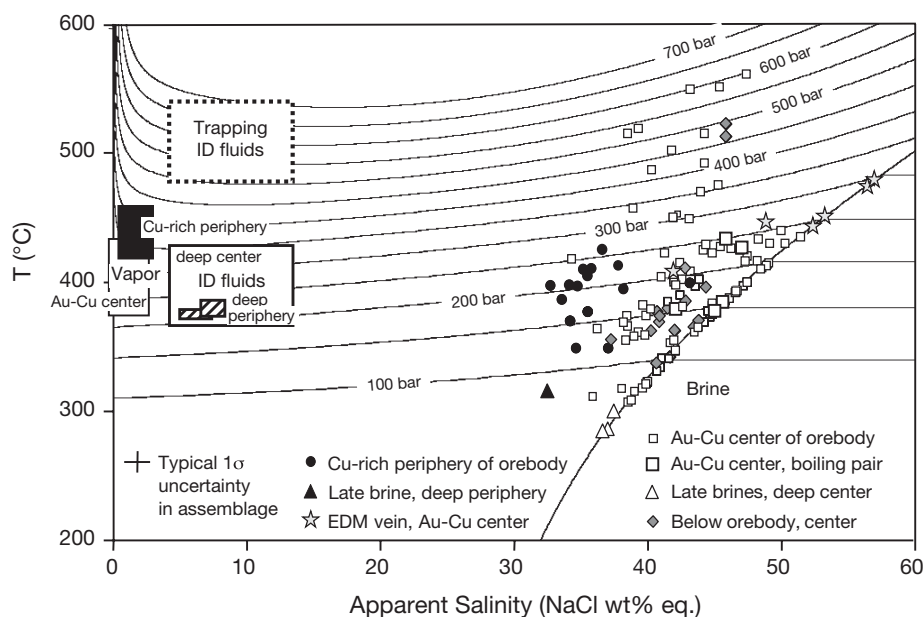
FIG. 9. Summary of microthermometric data, showing salinity in wt percent NaCl equiv vs. temperature of final homogenization; salinities determined from halite dissolution (Bodnar and Vityk, 1994; brine inclusions, type B) and rare observations of clathrate melting constrained by liquid CO$_2$ in ID and V type inclusions (Fig. 8); each point symbol represents one assemblage, usually averaging several individual inclusion measurements; fine background lines are isobars of the limiting two-phase (brine + vapor) surface and the halite saturation limit of the NaCl-H$_2$O model system (after Driesner and Heinrich, 2007).

In contrast to the generally small intermediate-density inclusions, the vapor inclusions are commonly large with a big and easily observable bubble. A single assemblage contained sufficient CO_2 to allow homogenization as well as clathrate temperatures to be measured, yielding a poorly defined low salinity of 0.9 ± 1 wt percent NaCl equiv. Many other vapor assemblages show clathrate melting between 4.4° ± 0.4° and 7.4° ± 0.3°C, without evidence of liquid CO_2 despite good visibility and careful observation, which indicates that they also have low salinities (less than ~4 wt % NaCl equiv; Fig. 8). Final homogenization occurs by bubble expansion but was not systematically measured, because only minimum temperatures are observable.

Brine inclusion (type B) data are plotted in Figure 9 as temperature of final homogenization versus apparent salinity in wt percent NaCl equiv, whereby each point symbol represents the average from an assemblage of 1 to 12 individual inclusion measurements. Uncertainty within one assemblage is typically ±2 wt percent NaCl equiv and ± 8°C in T_h. The total range in salinity and homogenization temperature varies from 32 to 57 wt percent NaCl equiv and from 260° to 550°C, respectively. This is much greater than within-assemblage uncertainty, demonstrating true geologic variations. Most of the inclusion assemblages from the central Au-Cu orebody (Au-Cu center, Fig. 2) homogenize by vapor disappearance into the liquid, but there are also many assemblages, especially at the lower temperature end of the range, that finally homogenize by halite dissolution after bubble disappearance. Unambiguous boiling trails with coexisting brine and vapor inclusions commonly show almost simultaneous disappearance of halite and bubble to a homogeneous liquid, suggesting transient halite saturation in the central Au-Cu orebody. This would constrain the trapping conditions to a low pressure of ~150 bars at ~380°C (Fig. 9, lowermost large squares). The highest temperatures are observed in early brine assemblages trapped in presulfide Q1 quartz of the high-grade Au-Cu–rich center, but we have no petrographic record of whether they coexisted with associated vapor inclusions (Redmond, 2002). Brine salinities in the center cluster at 45 ± 5 wt percent NaCl equiv, whereas brines in the Cu-rich periphery are of lower salinity on average (35 ± 4 wt % NaCl equiv) but homogenize at similar temperatures (340°–420°C) as the majority of assemblages in the Au-Cu–rich center. These lateral salinity differences are consistent with the petrographic observations of higher salt proportions in the Au-Cu–rich center, compared to the periphery (Fig. 7). Rare boiling-trail assemblages (too small for quantitative measurement) indicate that some fluids in the Cu-rich peripheral orebody were also trapped in the two-phase field of coexisting liquid + vapor but well below halite saturation (Fig. 9).

A thin EDM veinlet within QMP contains brines with the highest of all observed salinities but without clearly coeval vapor inclusions. Final homogenization by halite dissolution as high as 450°C indicates salinities up to 58 wt percent NaCl equiv (Fig. 9), but larger than usual variation within assemblages may indicate postentrapment modification of these petrographically early inclusions.

Brine inclusions in quartz-molybdenite veins were not studied in detail and are omitted from Figure 9. Microthermometric data overlap the range of inclusion properties in quartz stockwork veins in the central region (digital supplement).

Two-phase aqueous (type A) inclusions are minor but widespread as secondary inclusions in all veins, demonstrably postdating Q2 quartz in stockwork vein samples studied by CL. They are the predominant and locally primary inclusions associated with the dull-luminescent third quartz of late quartz-pyrite veins with sericitic alteration (QSP veins: Fig. 5I). Phase proportions and reconnaissance measurements indicate low salinity and homogenization temperatures of ~320°C or lower.

Elemental composition of fluids

Cation ratios relative to Na, determined by LA-ICPMS microanalysis, are plotted in Figure 10 (two-phase inclusions of types ID, V and A) and Figure 11 (brine inclusions). Each point represents one inclusion assemblage, with error bars denoting 1σ variation of individual inclusions in the assemblage. Data are sorted first according to sampling region, then by sample and veining stage. Within one sample, data are sorted arbitrarily by decreasing Cu/Na ratio. Estimates of fluid compositions in different regions of the deposit are given in Tables 2 and 3, based on a combination of LA-ICPMS measurements of metal ratios, microthermometric data, and mass-balance constraints based on the interpreted fluid evolution (below).

The concentration ratios among most major and trace elements are essentially constant throughout all generations of fluid inclusions. This is particularly prominent in the brine inclusions where the LA-ICPMS signals are strong and reproducibility within one assemblage is best. Also among two-phase (types ID, V and A) inclusions, there are no systematic differences in concentration ratios among Na, K, Fe, Mn, Zn, Pb, Rb, Cs, and additional elements analyzed close to their detection limit (Ca, Ba, Sr, and possibly As, W).

By contrast, the main ore-forming metals Cu, Mo, and probably also Au show significant variations between assemblages in each sample and also from sample to sample between different regions. Copper is a major component besides Na, K, and Fe in type ID, B, and V fluids and is even the dominant cation element in some vapor inclusion assemblages (Cu/Na >1). Cu/Na varies over three orders of magnitude, even in single samples. This variation is geologically real, being much greater than the variability within one assemblage (although the within-assemblage variation in Cu/Na is generally greater than between other cations; note error bars in Figs. 10 and 11). Copper concentration in brine inclusions correlates with the temperature of final homogenization for those inclusion assemblages in sample D211-19 that could be associated with the early quartz generation Q1 (Landtwing et al., 2005; see discussion below). Molybdenum concentrations are much lower and not as well defined, but Mo/Na and also the ore metal ratio Mo/Cu seem to reach their highest values in some of the fluid inclusion assemblages from quartz-molybdenite veins. Gold is invariably close to the detection limit and only detected in some inclusions in each assemblage. This creates an ambiguity in averaging of results, as the clearly detected gold signals in each assemblage are likely to be at the upper end of the true analytical variation within the assemblage. A statistical tendency to overrepresent the highest values is also indicated by the individually calculated limits of detection, expressed as maximum Au/Na
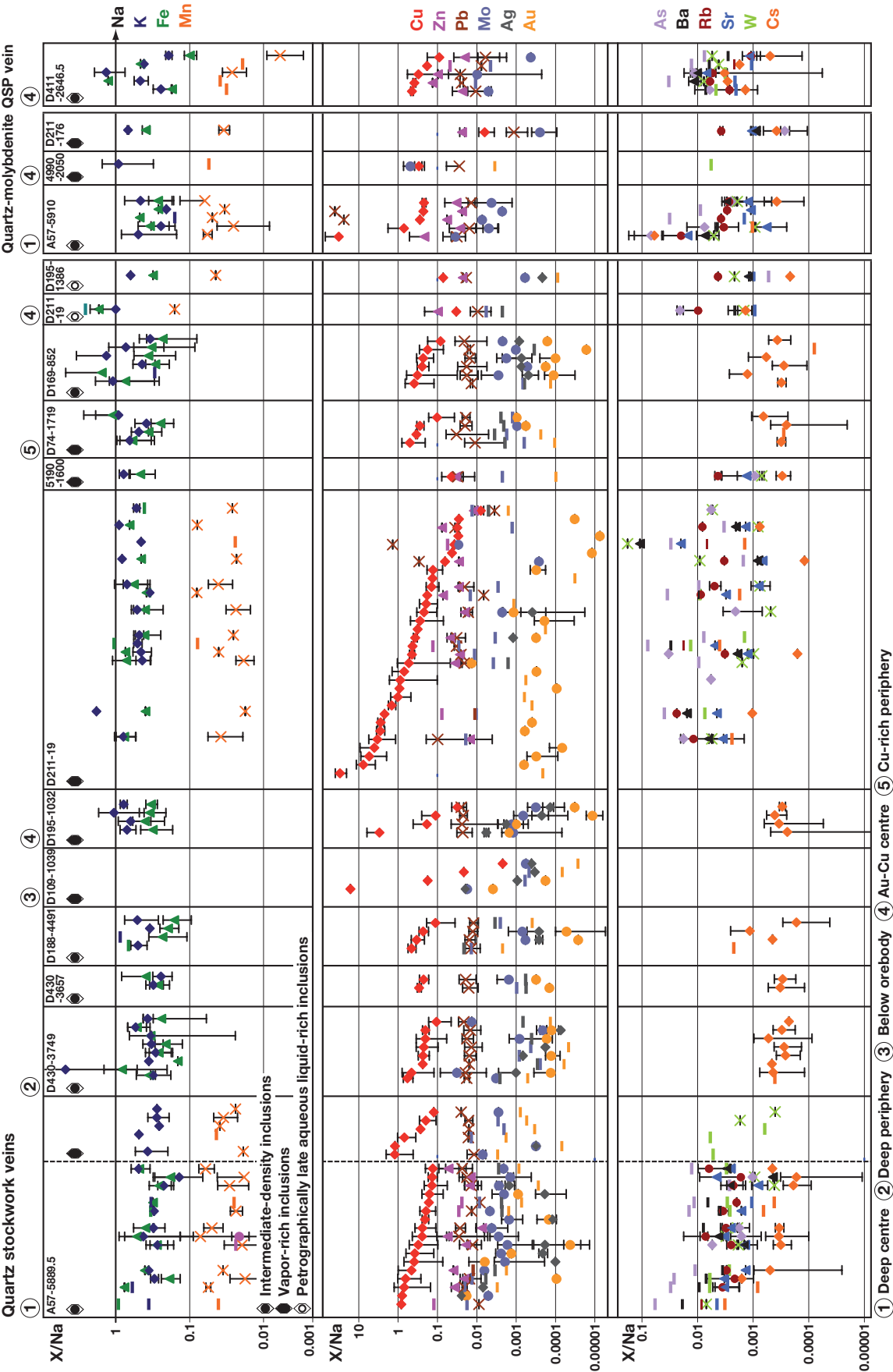
FIG. 10. Element ratios X/Na for two-phase fluid inclusion assemblages (types ID, V, and A) in stockwork veins from different regions of the system (Fig. 2, Table 1; digital supplement). Also shown are type V inclusions from two molybdenite veins and aqueous liquid inclusions (type A) in a late quartz-pyrite (QSP) vein. Each symbol represents one assemblage, averaged from 1 to 15 values measured above the detection limit, which is calculated for each element in each inclusion (Heinrich et al., 2003). Error bars indicate 1σ where two or more values were determined. Within one sample, assemblages are arbitrarily sorted by decreasing Cu/Na.

FIG. 11. Summary of microthermometric data (top panel) and element ratios X/Na for brine inclusion assemblages (type B) in an EDM vein, in stockwork veins from different regions of the ore system (Fig. 2, Table 1; digital supplement), and in molybdenite veins from the center of the orebody, sorted by decreasing Cu/Na within each sample. Error bars indicate 1σ of several inclusions in one assemblage. Element ratios are plotted for easier comparison with the two-phase inclusions shown in Figure 10 but relate more closely to absolute concentrations, as total salinities of the brines vary within less than a factor of two.

in each inclusion, which are commonly smaller for some inclusions than the calculated average of Au/Na ratios of detected gold signals. However, gold is unquestionably present as an inclusion component at a concentration ratio of Au/Na $\sim 10^{-5\pm1}$, but variations within this uncertainty range may not be geologically significant.

Comparing brine and vapor inclusions in samples containing both fluid inclusion types, the vapors are on average enriched in Cu/Na compared with the brines. Figure 12 shows the data from a single boiling trail, i.e., from strictly coeval brine and vapor inclusions trapped on a single healed microfracture in Q1 quartz from the central Au-Cu orebody (sample D211-19; Table 1, digital supplement). Both fluids contain high Cu/Na, but the vapor inclusions are enriched in Cu relative to Na and all other metals. The majority of individual vapor inclusions on this trail contain Cu as the most abundant metal. Au also tends to fractionate in favor of the vapor phase, relative to Na, but only a few analyses returned detectable signals, leading to large uncertainty. Additional boiling trail data are reported in Seo et al. (2009), showing high Cu, Au, as well as S concentrations in both fluid phases and a correlated enrichment of all three ore-forming elements relative to Na in the vapor.

Interpretation and Discussion

The fluid inclusion data together with geologic observations documented in Redmond et al. (2001), Redmond (2002), Redmond and Einaudi (2010), and Gruen et al. (2010) can explain the origin of the zoned ore shell of the Bingham Canyon
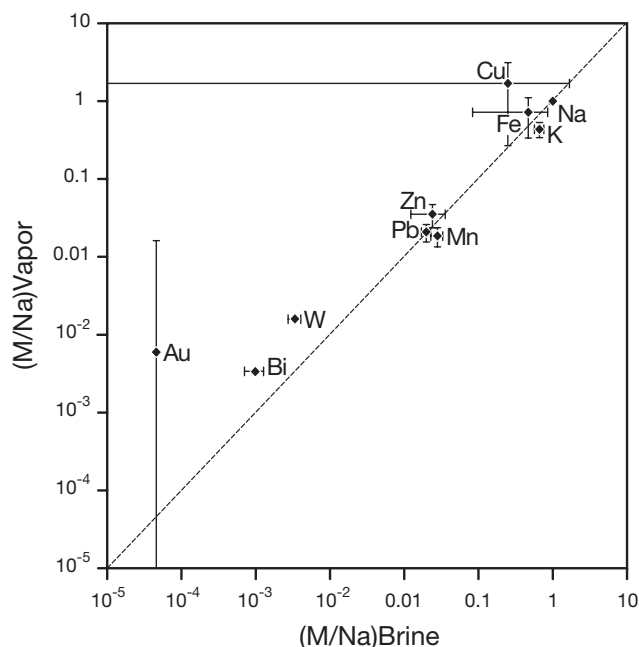

FIG. 12. Element ratios X/Na in vapor plotted against the corresponding concentration ratio in brines from a high-temperature (426°C) boiling trail in Q1 quartz from the stockwork vein D211-19, trapped on a single healed crack and representing a two-phase fluid at the onset of bornite-chalcopyrite precipitation. Although Cu concentrations are variable and Au was only detected in a few of the inclusions, the vapor is enriched in these ore metals relative to the brine and contains Cu as the predominant cation (Cu/Na > ~1 corresponding to a concentration of ~1 wt % Cu in the vapor).

deposit. Deposit-scale variation of Au/Cu ratio in the ore is explained by slightly different evolution paths of a common input fluid ascending through a broad column of fractured rock extending well beyond the QMP. The single-phase input fluid was initially hot and under lithostatic pressure, with high Au and Cu contents controlled by a deep igneous source. Portions of this fluid ascending along the central zone of highest permeability expanded above the transition from lithostatic to hydrostatic fluid pressure, resulting in wholesale precipitation of both metals in the central high-grade Au-Cu orebody. Ore deposition occurred at low pressure, dominantly from the expanding vapor and to a lesser degree from minor condensing brine. Portions of similar fluid ascending in the periphery of the vein network cooled at slightly higher pressure and underwent less extreme phase separation, resulting in selective copper precipitation in the deeper peripheral ore zones. The following sections discuss key aspects of the proposed process and place them into the broader context of porphyry copper ± gold ore formation.

One homogeneous deep input fluid

The input fluids to the main stage of Cu ± Au mineralization were sampled ~3 km below the land surface at the time of mineralization (Fig. 2; Deino and Keith, 1997; Waite et al., 1997; Gruen et al., 2010, fig. 1C). The intermediate-density (type ID) inclusions trapped a single-phase fluid at near-lithostatic pressure, estimated to be around 820 bars based on the stratigraphic overburden. Homogenization to vapor or by meniscus fading at 400° ± 30°C and an apparent salinity of ~7 wt percent NaCl equiv are inconsistent with the binary NaCl-H_2O model system in which a fluid of such high salinity would homogenize into the liquid phase (Fig. 9; Driesner and Heinrich, 2007). Estimating the actual trapping temperature of the deep input fluid requires a pressure correction, which is difficult to calculate given this compositional complexity. The isochore of a 7 percent NaCl liquid homogenizing at 400° ± 30°C provides a likely minimum correction, as the isochores of a CO_2-bearing vapor-homogenizing fluid would have a somewhat lower dP/dT slope. Using the SoWat isochore equations of Driesner and Heinrich (2007) for the binary model system yields a fluid density of 0.59 ± 0.07 g cm^{-3}, in good agreement with the graphically determined average of 0.63 in sample A51-4788 (Fig. 7). Following this isochore to ~820 bars yields a temperature correction of about 90°C. Added to the range of measured homogenization temperatures, this correction defines the minimum trapping conditions of the deep input fluid, at ≥450° to 520°C in the single-phase stability region (Fig. 9).

The elemental composition of the input ore fluid is summarized in Figure 13, comparing the ranges between intermediate-density inclusion assemblages from the barren deep center below the Au-Cu orebody with those from the deep periphery at the base of the Cu-rich peripheral ore zone. Even excluding some outliers, the deep single-phase fluids from both regions have overlapping composition in terms of conservative elements like K, Pb, or Cs, as well as the ore-forming elements Cu, Mo, Ag, and Au. Copper in deep intermediate-density inclusion assemblages varies significantly in totally Cu-Fe sulfide-free samples, and the Cu/Na variation even within one assemblage is commonly greater than other
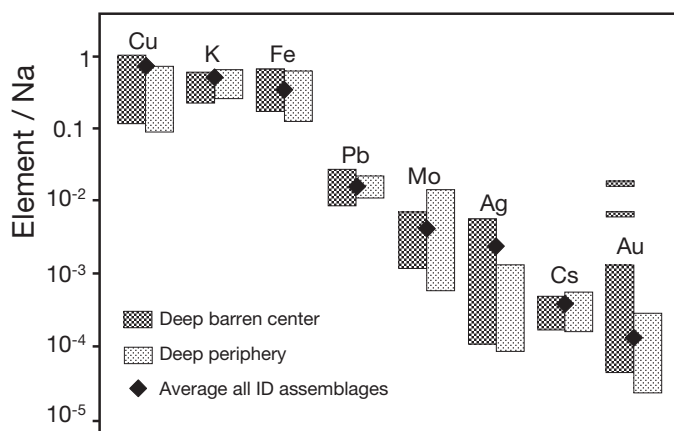
FIG. 13. Ranges of element ratios in intermediate-density (type ID) inclusion assemblages, showing that deep input fluids in the center and at the periphery of the ore system are indistinguishable, regarding ore metals (Cu, Mo, Ag, Au) as well as conservative elements in the porphyry orebody reflecting unmodified source characteristics (K, Fe, Pb, Cs). Small diamonds indicate averages of all assemblages used as common input fluid for the mass-balance calculation in Tables 2 and 3 (first columns), except for Cu where the average of three consistently high assemblages used to account for incipient sulfide precipitation, and excluding very high Au outliers (possibly due to trapped microparticles).

major cation ratios. This variation could indicate variation in fluid source composition or incipient phase separation, or be due to some postentrapment diffusive reequilibration of cation ratios in these high-temperature inclusions (Li et al., 2009; Zajacz et al., 2009). Gold was clearly detected in the inclusions from the deep periphery, showing that the peripheral input fluids were not inherently Au poor compared with those deep below the Au-Cu center of the deposit. Comparing the average Au content of all deep intermediate-density–type fluid inclusions with the upper end of the range of Cu values yields an Au/Cu ratio of ~10^{-4}. This value is close to the bulk ore Au/Cu ratio of $0.8\cdot10^{-4}$ contained within the Au-Cu center of the orebody (inside the >0.6 g/t Au contour; Gruen et al., 2010).

Phase separation by condensation of minor brine

The mapped transition from intermediate-density inclusions in deep quartz stockwork veins to the ubiquitous association of brine and vapor inclusions higher up (Fig. 7) is interpreted as a phase separation front within an ascending fluid plume. The upward-concave shape of this front, the variable phase proportions in the inclusions at room temperature (Fig. 7), and the microthermometric data from associated and locally coexisting vapor and brine inclusions (Fig. 9) can be interpreted by comparison with the two-phase stability surface ("solvus") of the NaCl-H_2O model system (thin isobars shown in Fig. 9 from Driesner and Heinrich, 2007).

The data indicate different degrees of phase separation between the center and the periphery of the fluid plume, which is very sensitive to pressure in this pressure-temperature region. In the center, phase separation was most extreme, leading to highly saline brine coexisting with a vapor of low density and low salinity. The observations indicate a wide gap of fluid unmixing in the central upflow zone, at pressures of

~100 to 200 bars. Brine and vapor inclusions in the Cu-rich periphery of the deposit are more similar in density (Fig. 7) and salinity (Figs. 8, 9). Thus, brine and vapor in the periphery were trapped at conditions where the two-phase region was narrower, implying higher pressures of ~200 to 300 bars at similar temperatures of 350° to 420°C. These spatial differences in fluid pressure are likely to be real, even though the absolute pressure-temperature determinations are not well defined. Individual boiling trails potentially give more precise measurements of pressure-temperature conditions, but minor unquantified CO_2 and salts other than NaCl also lead to uncertainties up to 100 to 200 bars (e.g., Liebscher, 2007).

The spatial variation of fluid density and composition in the Bingham Canyon system indicate upflow and phase separation along a steep decompression gradient below the Au-Cu–rich center of the orebody. By contrast, originally similar fluids ascending along the Cu-rich periphery of the orebody followed a more gentle decompression and fluid-separation path. Mass-balance calculations shown in Tables 2, 3, and Figure 14 confirm that the interpreted phase separation of a deep single-phase fluid into brine and vapor is consistent with all analytical constraints, not only regarding total salinity but also for all analyzed element ratios. The two tables list best-fit results from a spreadsheet model based on mass conservation for all components, using assumptions that are detailed in footnotes to Table 2 (Excel spreadsheet in digital supplement). We take as given the average apparent salinity of the brines (in wt % NaCl equiv), the empirical approximation for the effect of other salts upon microthermometric behavior (Heinrich et al., 2003), and the average element ratios
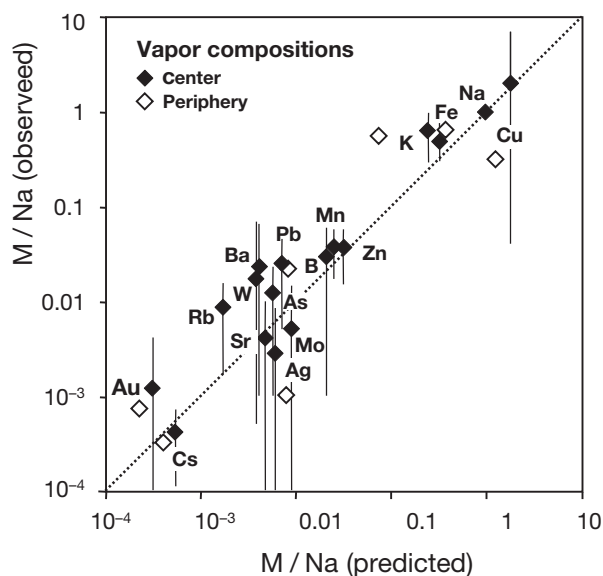
FIG. 14. Ore-forming vapor compositions, comparing analytical observation with predictions from mass balance during phase separation in the central upflow zone (full symbols) and in the Cu-rich periphery (open symbols, limited data). Observed element ratios in vapor inclusions from the two regions are plotted against the predicted vapor composition (Tables 2, 3) that would result from subtraction of 10 mass units (X = 0.10) of analyzed brines from 100 mass units of single-phase intermediate-density fluid (indistinguishable composition in the deep barren center and at the base of the peripheral copper orebodies; see Fig. 13 and text for discussion).

TABLE 2. Best-Estimate Ore Fluid Compositions in the Stockwork Vein Stage in the Central Upflow Zone and the Au-Cu Orebody Prior to Au and Cu-Fe Sulfide Saturation

Compositions are calculated with a spreadsheet to be consistent with a common input fluid based on the average element ratios in intermediate-density fluids measured by LA-ICPMS (column c), followed by phase separation into brine and vapor; brine composition is based on averaged analyses of inclusion from the deposit center (columns e, f), and the vapor is calculated by mass-balance (columns h, i) and compared with analyzed element ratios (column l); see footnotes for calculation, Figure 13 for comparative plot, and text for discussion

| | | Intermediate-density fluid analyzed (avg all ID) App Sal % NaCl equiv 7.0 / Na wt % = 1.97 | | Brine analyzed (avg all B below orebody) App Sal % NaCl equiv 45.0 / Na wt % = 11.87 | | | Vapor predicted (100 g ID fluid − X × 100 g brine) App Sal % NaCl equiv 3.88 / Na wt % = 0.87 | | Fluid mass fraction 1-X 0.90 | | Vapor analyzed (avg all V) Uncertainty 1σ | |
Component (a)	MMCl/MM (b)	El ratio M/Na (ICP) (c)	Concentration wt % (gMCl/100g ID) (d)	El ratio M/Na (ICP) (e)	Concentration wt % (gMCl/100g B) (f) Fluid mass fraction X 0.10	Component fraction (g)	El ratio M/Na (pred) (h)	Concentration wt % (gMClx/100gV) (i)	Component fraction (k)	El ratio M/Na (ICP) (l)	+ (m)	− (n)
NaCl	2.5421	1	4.9963	1	30.165	3.0165	1	2.1998	1.9798	1	0.3400	0.3400
KCl	1.9067	0.5500	2.0611	0.7500	16.969	1.6969	0.2453	0.4047	0.3642	0.6300	0.1600	0.1600
FeCl2	2.2696	0.3500	1.5613	0.3800	10.234	1.0234	0.3043	0.5976	0.5379	0.4900	0.0200	0.0200
MnCl2	2.2907	0.0380	0.1711	0.0470	1.2775	0.1278	0.0243	0.0481	0.0433	0.0370	0.0200	0.0200
Cu	1	0.7500	1.4741	0.0630	0.7476	0.0748	1.7967	1.5548	1.3993	1.9400	5.0500	1.9000
ZnCl2	2.0847	0.0290	0.1188	0.0270	0.6679	0.0668	0.0320	0.0578	0.0520	0.0360	0.0210	0.0210
PbCl2	1.3422	0.0166	0.0438	0.0228	0.3631	0.0363	0.0072	0.0083	0.0075	0.0250	0.0200	0.0200
Mo	1	0.0043	0.0085	0.0012	0.0142	0.0014	0.0090	0.0078	0.0070	0.0051	0.0094	0.0050
AgCl	1.3287	0.0025	0.0065	0.0002	0.0032	0.0003	0.0061	0.0069	0.0062	0.0028	0.0056	0.0027
Au	1	0.0001	0.0003	0.0000	0.0002	0.0000	0.0003	0.0003	0.0002	0.0012	0.0029	0.0011
Rb	1.4148	0.0034	0.0095	0.0045	0.0755	0.0076	0.0017	0.0021	0.0019	0.0085	0.0068	0.0068
Ba	1.5163	0.0023	0.0069	0.0011	0.0198	0.0020	0.0041	0.0054	0.0049	0.0230	0.0420	0.0220
Sr	1.8092	0.0025	0.0089	0.0010	0.0215	0.0021	0.0048	0.0075	0.0067	0.0041	0.0058	0.0040
W	1	0.0025	0.0049	0.0014	0.0166	0.0017	0.0039	0.0036	0.0033	0.0170	0.0520	0.0165
As	1	0.0025	0.0049	0.0003	0.0036	0.0004	0.0058	0.0051	0.0046	0.0120	0.0110	0.0110
Cs	1.2668	0.0004	0.0010	0.0003	0.0045	0.0005	0.0006	0.0006	0.0005	0.0004	0.0003	0.0003
B	1	0.0091	0.0178	0.0012	0.0142	0.0014	0.0211	0.0183	0.0164	0.0300	0.0290	0.0290
			TDS wt % 10.4777		TDS wt % 60.5827			TDS wt % 4.9105				

Calculation procedure and assumptions (all data in wt units; absolute concentrations in wt %, i.e., grams per 100 g fluid; see digital supplement)

1. Element ratios M/Na in columns (c) and (e) are assemblage averages directly form LA-ICPMS analysis: (c) = all ID from deep barren center and deep periphery Cu average from three consistently high assemblages (low values in range may indicate incipient sulfide deposition); outlying high Au values (microparticles?) omitted; values in (e) are all brines from stockwork veins below the Au-Cu orebody, i.e., after phase separation but prior to significant Cu-Au deposition

2. Apparent salinity (wt % NaCl equiv) shown as bold figures near top of columns (d) and (f) are adjusted for best fit within the ranges indicated by microthermometry; values of 7 ± 2 for ID fluid and 45 ± 3 for brines predict positive concentrations in vapor (column i), and predicted ratios (h) in agreement with analyses (column l)

3. Na wt % (italics, top of d, f) computed from NaCl wt % equiv (apparent salinity, bold) by empirical correction, using conversion factors (b) and analyzed ratios M/Na: Na wt % = NaCl wt % equiv/[MNaCl/MNa + 0.5*Σ(M/Na*MMCl/MM)] summed over all major components except Cu (Heinrich et al., 2003)

4. Absolute concentrations (columns d, f) of all salts or elements (column a) are calculated from element ratios (c, e) and the absolute Na wt % concentration

5. Assuming mass fractions of Brine (X) and Vapor (1-X) by splitting 100 g of ID fluid, predict fraction of each component in Vapor (k) by difference: component fraction in Vapor (in grams, column k) = component concentration wt % in ID fluid (column c) − component fraction separated into Brine (column g)

6. Back-calculate (k) into concentrations of each component in Vapor (column i) and predicted element ratios of Vapor (column h); TDS = total disolved salts

7. Adjust apparent salinities of ID and B for positive values of predicted element ratios (h) and compare with analyzed element ratios (l = avg all V in center; ± uncertainties of analyzed vapors + 1σ, −1σ or estimated lower value >0); check whether apparent salinity is consistent with microthermometry (<4 wt % NaCl equiv)

TABLE 3. Best-Estimate Ore Fluid Compositions in the Stockwork Veins of the Peripheral Cu Ore Shell

Calculated in same way as Table 2 and based on the same intermediate-density input fluid, but lower salinity brine inclusions as observed in peripheral parts of the system

Component (a)	MMCl/MM (b)	Intermediate-density fluid analyzed (avg all ID) Na wt % = 1.97		Brine analyzed (avg all B in Cu-rich periphery) Na wt % = 8.60			Vapor predicted (100 g ID fluid — X × 100 g brine) Na wt % = 1.23				Vapor analyzed (avg all V)	
		El ratio M/Na (ICP) (c)	Concentration wt % (gMCl/100g ID) App Sal % NaCl equiv 7.0 (d)	El ratio M/Na (ICP) (e)	Concentration wt % (gMCl/100g B) App Sal % NaCl equiv 36.0 (f)	Component fraction Fluid mass fraction X 0.10 (g)	El ratio M/Na (pred) (h)	Concentration wt % (gMClx/100gV) App Sal % NaCl equiv 5.34 (i)	Component fraction Fluid mass fraction 1-X 0.90 (k)	El ratio M/Na (ICP) (l)	Uncertainty 1σ + (m)	– (n)
NaCl	2.5421	1	4.9963	1	21.850	2.1850	1	3.1238	2.8115	1		
KCl	1.9067	0.5500	2.0611	0.8111	13.293	1.3293	0.3471	0.8132	0.7319	0.6100	0.2400	
FeCl$_2$	2.2696	0.3500	1.5613	0.6918	13.496	1.3496	0.0844	0.2353	0.2118	0.5700	0.3800	0.3800
MnCl$_2$	2.2907	0.0380	0.1711	0.0329	0.6484	0.0648	0.0422	0.1189	0.1070	n.d.		
Cu	1	0.7500	1.4741	0.1740	1.4954	0.1495	1.1977	1.4717	1.3246	0.3100	0.1600	0.1600
ZnCl$_2$	2.0847	0.0290	0.1188	0.0253	0.4524	0.0452	0.0314	0.0804	0.0724	n.d.		
PbCl$_2$	1.3422	0.0166	0.0438	0.0266	0.3065	0.0307	0.0089	0.0146	0.0131	0.0210	0.0090	0.0090
Mo	1	0.0043	0.0085	0.0002	0.0021	0.0002	0.0075	0.0092	0.0082	0.0009		
AgCl	1.3287	0.0025	0.0065	0.0003	0.0029	0.0003	0.0043	0.0069	0.0062	n.d.		
Au	1	0.0001	0.0003	0.0000	0.0002	0.0000	0.0002	0.0003	0.0002	0.0008	0.0003	0.0003
Rb	1.4148	0.0034	0.0095	0.0045	0.0542	0.0054	0.0026	0.0045	0.0040	n.d.		
Ba	1.5163	0.0023	0.0069	0.0009	0.0111	0.0011	0.0034	0.0064	0.0057	n.d.		
Sr	1.8092	0.0025	0.0089	0.0010	0.0157	0.0016	0.0037	0.0081	0.0073	n.d.		
W	1	0.0025	0.0049	0.0008	0.0072	0.0007	0.0035	0.0047	0.0042	n.d.		
As	1	0.0025	0.0049	0.0005	0.0045	0.0004	0.0039	0.0050	0.0045	n.d.		
Cs	1.2668	0.0004	0.0010	0.0005	0.0052	0.0005	0.0003	0.0005	0.0005	0.0004	0.0002	0.0002
B	1	0.0091	0.0178	0.0027	0.0230	0.0023	0.0141	0.0173	0.0155	n.d.		
		TDS wt %	10.4955	TDS wt %	51.6680		TDS wt %	5.9207				

analyzed in the intermediate-density and the brine inclusions, whereby the maximum Cu/Na of the brines was taken to represent the phase-separated fluid prior to Cu-Fe sulfide precipitation. We then varied the apparent salinity of the intermediate-density fluids within their possible limits and the unknown mass fractions of vapor/brine formed by separation of a given amount of intermediate-density fluid. For selected values for these two parameters, the resulting salinity and all metal concentrations of the vapor are predicted by the model and can be compared to the plausible salinity range and analyzed element ratios in the vapor inclusions (Fig. 14).

The mass balance on phase separation was calculated independently for the interpreted central upflow zone (Table 2) and for the periphery of the system (Table 3), taking into account the observed difference in average brine salinity of 45 and 36 wt percent NaCl equiv, respectively. Results showed that only a limited range of input salinity and vapor/brine ratio satisfy all constraints, without predicting negative concentrations of some elements or salinities outside the range permitted by microthermometric data. The independently predicted vapor compositions are therefore well constrained, and the results agree with the analyzed inclusion compositions (Fig. 14).

Both in the center and in the periphery, the best fit is achieved assuming a phase ratio of vapor/brine of approximately 9/1. Including the modeling uncertainty of this ratio, we conclude that 100 g input fluid of intermediate density separated into 90 ± 3 g vapor and 10 ± 3 g brine during ascent. To achieve a plausible fit, the starting salinity of the intermediate-density fluids had to be 7 ± 2 wt percent NaCl equiv, corresponding to 8 to 13 wt percent total dissolved salts. Total salinity of the vapor ascending through the central Au-Cu orebody is computed to be about half the salinity of the single-phase input fluid, whereas in the periphery the vapor is closer in salinity to the input fluid. The higher predicted vapor salinity in the Cu-rich periphery and the lower salinity of the associated brines (determined by microthermometry, Fig. 9) are consistent with the phase proportion statistics (Fig. 7), indicating a narrower two-phase region at slightly higher pressure and/or lower temperature compared to the Au-Cu center of the system. Element/Na ratios in the predicted vapor agree with the vapor inclusion analyses within their overall variability, with regard to all well-defined elements including the main ore metals Cu, Mo, and Au. Prior to the onset of Cu-Fe sulfide precipitation, the vapor contains Cu as its most abundant metal component, in agreement with the most copper rich assemblages in the broad range of analyses. The high mass fraction of vapor and its high Cu content imply that 95 percent of the total copper was deposited by the vapor phase. In the periphery, the observed Cu content of the inclusions is smaller than the prediction, probably reflecting the smaller data set and the fact that chalcopyrite is already precipitating at greater depth, possibly prior to phase separation (Figs. 10, 11). Detectable gold in intermediate-density and vapor fluid inclusions from the deep periphery and from the Cu-rich but Au-poor peripheral ore zone indicates that gold is transported through the peripheral upflow region, without precipitating within the current mine volume.

The physical process of phase separation depends on whether the input fluid breaches the two-phase surface on the liquid side or on the vapor side of the critical curve (e.g., Liebscher and Heinrich, 2007). A homogeneous fluid with initially 7 wt percent salinity, ascending from 800 bars at any temperature greater than ~450°C, will first intersect the two-phase curve on the vapor side of the critical curve (Fig. 9). Therefore, phase separation at Bingham Canyon occurred not by boiling (i.e., formation of vapor bubbles from a liquid) but rather by condensation of droplets of hypersaline brine from the dominant vapor.

Sulfide precipitation during quartz dissolution

Cathodoluminescence textures of ore samples consistently show that chalcopyrite and bornite precipitated into secondary pore space, created by dissolution of the main vein-forming quartz generation Q1 (Redmond et al., 2004). Mineral textures in combination with fluid inclusion data, showing correlated decreases in temperature and Cu content of secondary fluid inclusion assemblages in Q1, indicate that Cu-Fe sulfide precipitation occurred during or immediately after Q1 dissolution. This was followed by recementation of the vein with a second quartz generation, Q2, during or after Cu-Fe sulfide precipitation (Landtwing et al. 2005).

Figure 15 links these textural observations with limited experimental solubility constraints. In pure water, quartz solubility decreases monotonically with falling temperature at pressures greater than ~750 bars (Kennedy, 1950; Fig. 15A). If the fluid is saline, this normal solubility dependence extends to lower pressures, as indicated by the gray isopleths in Figure 15A (Fournier, 1983). Quartz solubility in low-salinity fluids at low pressure shows a region of inverse temperature dependence, i.e., quartz solubility increases upon cooling from ~450° to ~350°C. We infer that most of Q1 in stockwork veins in and below the orebody probably precipitated upon cooling and decompression from >500°C and 800 bars to lower pressures and temperatures, as the fluids were ejected from the subjacent lithostatic fluid-pressure domain into an environment of hot hydrostatic conditions (Gruen et al., 2010). Based on equilibrium quartz solubility variation, this process will deposit 0.1 to 0.2 g of vein quartz per 100 g of hydrothermal fluid. Fluid packets experiencing decompression from 100 to 300 bars prior to cooling below ~450°C, as recorded by most of the fluid inclusion assemblages (Fig. 9), will pass through the region of retrograde solubility and therefore locally redissolve quartz. This explains the creation of secondary porosity in Q1 veins, prior to recementation with Q2 quartz (Fig. 5). In the two-phase region of brine + vapor coexistence, net quartz dissolution will result only if the low-salinity vapor predominates over the high-salinity brine; the brine by itself has no retrograde solubility even at low pressure (e.g., gray isopleth labeled 20% NaCl, Fig. 15A). We have not tried to quantify the combined effects of adiabatic expansion, cooling, and quartz solubility in a two-phase saline fluid mixture (cf. Akinfiev and Diamond, 2009), but the quartz dissolution textures are an independent qualitative confirmation that ore deposition in the Bingham Canyon system was dominated by magmatic vapor, rather than saline liquid.

Fluid pressure control on Au/Cu ore-grade zonation

The main difference between the Au-Cu–rich center and the relatively Cu-rich periphery of the system is in the slightly
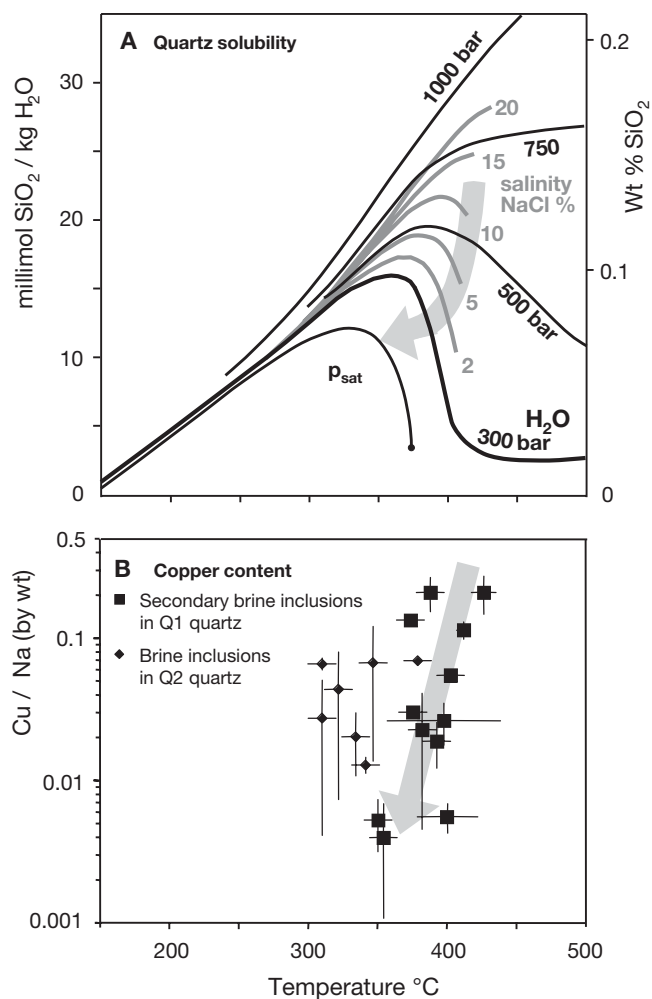
FIG. 15. Experimental quartz solubility as a function of pressure, temperature, and fluid salinity (A, based on data from Kennedy, 1950, and Fournier, 1983) and the observed evolution of copper content as a function of homogenization temperature in brine inclusion assemblages from sample D211-19 (B, redrawn in terms of element ratios from data in Landtwing et al., 2005, and digital supplement). The arrows indicate how redissolution of the previously deposited main generation of vein quartz (Q1; cf. Fig. 5) and Cu precipitation have occurred together in the same cooling interval, from a predominant low-salinity fluid of vaporlike density.

vapor density is the stabilization of metal ions and neutral complexes by hydration, i.e., by the formation of a shell of water molecules surrounding the metal-carrying species in the vapor. Although such experiments have not yet been completed for complex vapors in the Au-Cu-Fe-S-(O-H) system (cf. Zezin et al., 2008), the strong decompression and expansion of magmatic vapor ascending through the center of the fluid plume at Bingham Canyon is expected to lead to destabilization of transported metals, resulting in wholesale precipitation of most of the advected Cu and Au.

These experiments indicate that the most Au enriched and the highest grade center of the orebody was formed in the region of greatest fluid decompression. Indeed, the bulk Au/Cu ratio of this region approximately matches that of the input fluid composition, consistent with complete deposition of all advected copper and gold. Vapor expansion and separation of minor brine will be associated with adiabatic cooling of the fluid mixture. Indeed, a steep decrease of Cu content of associated brine inclusions is correlated with decreasing homogenization temperature of brine inclusion assemblages (Fig. 15B; modified from Landwing et al., 2005). Figure 10 (sample D211-19) shows that the vapor inclusions also record a decrease in Cu content over several orders of magnitude, starting from an even higher Cu/Na ratio compared with the brines (Fig. 11). Note that the temperature range of Cu-Fe sulfides precipitatation from ~430° to ~350°C (Fig. 15) is too low to initially incorporate all the gold in bornite solid solution (Simon et al., 2000; Redmond, 2002; cf. Kesler et al., 2002). This implies that native gold coprecipitated with copper iron sulfides in the Au-Cu–rich center of the orebody.

Fluids ascending along the periphery of the fluid plume remained denser, which favors the retention of Au in solution while copper is precipitating selectively. Even though solubility experiments are lacking to demonstrate this proposed metal separation, thermodynamic modeling of intermediate-density fluids and aqueous liquids (Heinrich, 2005) predict rapidly decreasing chalcopyrite solubility in any cooling S-rich fluid, while gold solubility remains high due to the formation of stable Au-HS complexes (Gammons and Williams-Jones, 1997; Stefánsson and Seward, 2004). High sulfur concentrations in the magmatic vapor at Bingham Canyon were recently confirmed by fluid inclusion analysis (Seo et al., 2009). Thus, we propose that the relatively gold poor but Cu rich periphery of the Bingham Canyon orebody formed by selective precipitation of chalcopyrite, while most of the advected gold was transported through and out of the porphyry orebody. Upon further cooling, the dense vapor can contract to an aqueous liquid and may eventually contribute to the formation of distal epithermal gold deposits such as Melco or Barney's Canyon (Sillitoe and Bonham, 1990; Cunningham et al., 2004). These deposits are small, but our interpretation implies that a much greater quantity of gold may have been lost from the system. This could amount to ~1,400 metric tons of "lost" gold if we assume that the Au/Cu ratio of the central Au-Cu orebody (0.8×10^{-4}) represents the bulk metal ratio of the input fluid and consider the known reserves of additional 19 Mt copper in Au-poor peripheral ore zones (Gruen et al., 2010).

Later fluids forming the quartz-molybdenite veins are compositionally similar to the quartz stockwork veins associated

different fluid evolution paths, which led to more extreme phase separation in the center compared to the periphery of the orebody. Volume expansion, phase separation, adiabatic cooling, and changing mineral solubilities in coexisting brine and vapor are all linked with each other but cannot be fully quantified for lack of thermodynamic data. Nevertheless, the combined observations and limited new experimetal data indicate that small differences in the density evolution of the cooling fluids could explain the zoned Au/Cu ratio in the Bingham Canyon orebody and the particularly high ore grades in the center of the system.

Experimental measurements of the solubility of metallic minerals in hydrous vapor have shown a strong positive correlation with the density of the vapor (Williams-Jones et al., 2002; Williams-Jones and Heinrich, 2005). At the atomic scale, the reason for increasing metal solubility with increasing

with Cu-Au mineralization (Figs. 10, 11), although some inclusion assemblages have slightly higher Mo/Na ratios. They seem to have experienced a similar pressure-temperature-phase evolution, without intermitttent cooling to the lower temperatures characterizing the quartz-pyrite veins with sericitic alteration. The latter contain aqueous inclusions with high Cu and Au contents, comparable to the transitional high-sulfidation epithermal fluids observed at La Famatina (Argentina; Pudack et al., 2009). These fluids, too, are potential source fluids for distal epithermal deposits.

Fluid flow and hydrology

The variation in fluid properties derived from inclusions in the quartz stockwork veins allow a qualitative interpretation of the flow pattern during Cu-Au mineralization at Bingham Canyon, consistent with the rock mechanical concept developed by Gruen et al. (2010). Figure 16 captures a schematic snapshot of a zoned magmatic fluid plume, indicating the varying density of vapor, intermediate-density fluids and liquids by variably dark shading. This cartoon is a gross simplification of a dynamic and locally very heterogeneous fluid-flow system. However, the observed large-scale mineral and inclusion zoning indeed requires a period of relatively stationary distribution of fluid pressure and temperature over several cycles of stockwork veining and Cu-Au mineralization.

A steep vertical gradient in fluid pressure and any lateral pressure difference between the center and the periphery of the fluid plume cannot be maintained in a stagnant hydrostatic environment. However, they can persist within a dynamic fluid plume—even under the extreme assumptions that rock permeability was similar across a broad upflow zone and that fluid pressure in the ore-depositing region was determined by the weight of the locally overlying fluid column. Such convective flow is predicted by hydrodynamic modeling (Driesner and Geiger, 2007), indicating that the center of a vapor-dominated two-phase fluid plume can maintain a relatively low pressure approaching vapor-static conditions. Vapor static means that pressure is determined dominantly by the integrated weight of upward-expanding low-density vapor and possibly overlying meteoric water. At the same time, the periphery of the magmatic fluid plume can be closer to hydrostatic condition, controlled by the weight of a more slowly flowing fluid mixture with overall higher density. The higher fluid density in the periphery of the plume is stabilized by two effects that mutually enhance each other: magmatic fluids cooling under elevated pressure maintains its density or even contracts to liquid (Heinrich et al., 2004), and elevated pressure is in turn maintained by the increasing density of the magmatic fluid, as well as liquid meteoric water convecting above the periphery of the fluid plume.

In reality, fluid pressure will additionally be affected by variable rock permeability. Fracture permeability varies due to hydraulic fracturing at the transition from near-lithostatic pressure conditions at depth, to pressure conditions closer to the Earth's surface that are determined by fluid density. Lithostatic fluid pressure prevails in the underlying source magma (below the solidus isotherm indicated schematically in Fig. 16) and probably extends upward into the broad region characterized by intermediate-density inclusions. The sharp base of the central Au-Cu orebody is interpreted as an
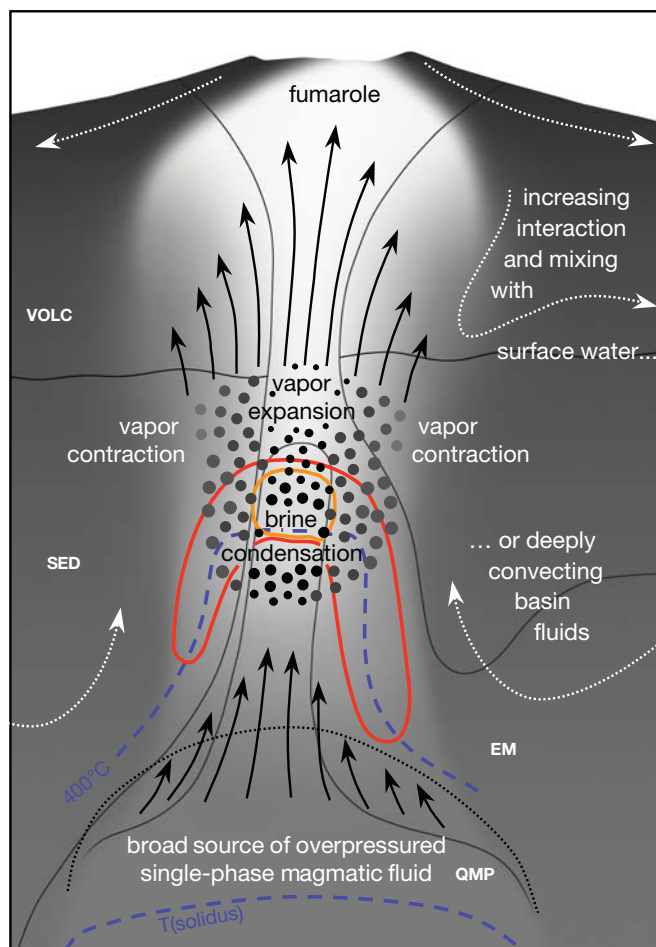

FIG. 16. Cartoon of the magmatic fluid plume that may have generated the zoned ore shell of the Bingham Canyon porphyry Cu-Au deposit, emphasizing the observed variations in fluid density by variable degrees of shading from low-density steam (white) to dense brine (black). The region of vapor density variation and local brine condensation is dominated by magmatic fluids, whereas the more evenly dark-gray surrounding may be dominated by surface-derived aqueous liquids. Interaction between magmatic and meteoric fluid is most likely in the near-surface fumarole environment where vapor will condense into ground water or at the periphery where contracted magmatic vapor becomes completely miscible with external aqueous liquids. Abbreviations: EM = equigranular monzonite, QMP = quartz monzonite porphyry, SED = sedimentary rocks, VOLC = volcanic rocks.

ore mineral saturation front within the overlying low-pressure domain, which probably remained relatively stationary for an extended period while fluids were continually advecting heat, sulfur, and metals through the vein network. The basal front of Cu-Au saturation probably approximates an isotherm surface near 430°C, based on the temperature of initial copper sulfide deposition indicated by Figure 15B (Landtwing et al., 2005). The thermal balance between fluid advection and heat loss required to maintain such a stationary saturation front is probably a key factor for generating the exceptionally high Cu and Au grades in the center of the Bingham Canyon orebody. Better understanding this dynamic stability in an inherently fluctuating high-energy environment will require quantitative evaluation of interacting physical and chemical processes (Steinberger et al., 2009; Weis et al., 2009).

The now eroded surface environment at the time of Cu-Au mineralization is open to speculation. The vapor plume may have reached the paleosurface as a giant fumarole or the vapor may eventually have mixed with near-surface water, e.g., in a laterally draining crater lake. Once copper-depleted but still gold-rich magmatic vapor ascending along the periphery of the fluid plume had contracted to an aqueous liquid below ~350°C, it would have become completely miscible with meteoric water. The mixed aqueous solution could have flowed laterally and downward depending on surface topography to contribute to the formation of sediment-hosted gold deposits. A downward-mineralizing flow path has been proposed by Cunningham et al. (2004) for the Melco deposit, located about 5 km north of Bingham Canyon, because this sediment-hosted epithermal deposit is conspicuously quartz poor and has no discernible fluid feeder zone in its footwall.

Conclusions

Geologic observations and fluid inclusion properties at Bingham Canyon extend the classic vapor plume model for magmatic-hydrothermal ore systems (Henley and McNabb, 1978) with specific conclusions regarding the hydrothermal geochemistry of porphyry Cu-Au ore deposition (cf. Williams-Jones and Heinrich, 2005).

The chemical mineralization efficiency and ore grade of porphyry Cu ± Au deposits is probably dominated by the sulfur chemistry of low-salinity magmatic fluids and the density evolution path of the fluids during cooling. Fluid inclusion analyses presented in this paper and by Rusk et al. (2004, 2008; Butte), Klemm et al. (2007; El Teniente) and Zajacz and Halter (2009; phenocryst inclusions in recent andesite) are in line with recently published experimental data on sulfide solubility and fluid partitioning (Nagaseki and Hayashi, 2008; Pokrovski et al., 2008), and with the discovery of high sulfur concentrations in metal-rich vapor inclusions (Seo et al., 2009). These data consistently indicate that the high Cu and Au concentrations found in many low-salinity magmatic fluids are controlled by sulfur as the dominant complexing ligand, rather than by chloride complexation as previously assumed.

The bulk Au/Cu ratio of porphyry-style ore deposits may be controlled at least partly by the vapor evolution process that explains the Au and Cu zoning within the porphyry ore shell at Bingham Canyon. The Au/Cu ratio of porphyry deposits empirically correlates with the depth and fluid pressure attending ore deposition (Cox and Singer, 1988; Sillitoe, 1997), as discussed by Murakami et al. (2009). Au-rich porphyry deposits in which Au and Cu coprecipitated at high temperature are typically formed at low fluid pressures in the subvolcanic domain, for example, Grasberg (MacDonald and Arnold, 1994), Bajo de la Alumbrera (Ulrich et al., 2002), and the porphyry gold deposits of the Maricunga belt (Vila and Sillitoe, 1991). By contrast, more deeply seated Cu ± Mo deposits are typically gold poor, for example El Teniente (formed from a low-salinity vapor intersecting the two-phase region near the critical curve or contracting directly to aqueous liquid; Klemm et al., 2007), or Butte (where ore deposition occurred at high pressure from a single-phase fluid; Rusk et al., 2004, 2008). Our model implies that, even if the input fluids into some of these Au-poor deposits contained some gold, copper was precipitated selectively due to the higher density of the cooling magmatic vapor. The nonprecipitating gold would ascend in the contracting vapor and be potentially available to form epithermal deposits at much shallower depth.

Acknowledgments

REFERENCES

Akinfiev, N.N., and Diamond, L.W., 2009, A simple predictive model of quartz solubility in water-salt-CO_2 systems at temperatures up to 1000° C and pressures up to 1000 MPa: Geochimica et Cosmochimica Acta, v. 73, p. 1597–1608.

Anderson, A.J., Clark, A.H., Ma, X.P., Palmer, G.R., Macarthur, J.D., and Roedder, E., 1989, Proton-induced X-ray and gamma-ray emission analysis of unopened fluid inclusions: ECONOMIC GEOLOGY, v. 84, p. 924–939.

Archibald, S.M., Migdisov, A.A., and Williams-Jones, A.E., 2002, An experimental study of the stability of copper chloride complexes in water vapor at elevated temperatures and pressures: Geochimica et Cosmochimica Acta, v. 66, p. 1611–1619.

Audétat, A., and Günther, D., 1999, Mobility and H_2O loss from fluid inclusions in natural quartz crystals: Contributions to Mineralogy and Petrology, v. 137, p. 1–14.

Audétat, A., Günther, D., and Heinrich, C.A., 1998, Formation of a magmatic-hydrothermal ore deposit: Insights with LA-ICP-MS analysis of fluid inclusions: Science, v. 279, p. 2091–2094.

Audétat, A., Pettke, T., Heinrich, C.A., and Bodnar, R.J., 2008, The composition of magmatic-hydrothermal fluids in barren and mineralized intrusions: ECONOMIC GEOLOGY, v. 103, p. 877–908.

Baker, T., Van Achterberg, E., Ryan, C.G., and Lang, J.R., 2004, Composition and evolution of ore fluids in a magmatic-hydrothermal skarn deposit: Geology, v. 32, p. 117–120.

Bodnar, R.J., 1995, Fluid-inclusion evidence for a magmatic source of metals in porphyry copper deposits: Mineralogical Association of Canada Short Course Series 23, p. 139–152.

Bodnar, J.R., and Vityk, M.O., 1994, Interpretation of microthermometric data for H_2O-NaCl fluid inclusions, *in* De Vivo, B., and Frezzotti, M.L., eds., Fluid iInclusions in minerals: Methods and applications: Blacksburg, VA, Virginia Technical Institute, p. 117–130.

Candela, P.A., and Holland, H.D., 1986, A mass-transfer model for copper and molybdenum in magmatic hydrothermal systems—the origin of porphyry-type ore deposits: ECONOMIC GEOLOGY, v. 81, p. 1–19.

Candela, P.A., and Piccoli, P.M., 1995, Model ore-metal partitioning from melts into vapor and vapor/brine mixtures: Mineralogical Association of Canada Short Course Series 23, p. 101–127.

Cathles, L.M., 1977, An analysis of the cooling of intrusives by ground-water convection which includes boiling: ECONOMIC GEOLOGY, v. 72, p. 804–826.

Cline, J.S., and Bodnar, R.J., 1991, Can economic porphyry copper mineralization be generated by a typical calc-alkaline melt: Journal of Geophysical Research-Solid Earth and Planets, v. 96, p. 8113–8126.

Cox, D.P., and Singer, D.A., 1988, Distribution of gold in porphyry copper deposits: U.S. Geological Survey Open-File Report 88–46, 23 p.

Cunningham, C.G., Austin, G.W., Naeser, C.W., Rye, R.O., Ballantyne, G.H., Stamm, R.G., and Barker, C.E., 2004, Formation of a paleothermal

anomaly and disseminated gold deposits passociated with the Bingham Canyon Porphyry Cu-Au-Mo system, Utah: Economic Geology, v. 99, p. 789–806.

Damman, A.H., Kars, S.M., Touret, J.L.R., Rieffe, E.C., Kramer, J., Vis, R.D., and Pintea, I., 1996, PIXE and SEM analyses of fluid inclusions in quartz crystals from the K-alteration zone of the Rosia Poieni porphyry-Cu deposit, Apuseni mountains, Rumania: European Journal of Mineralogy, v. 8, p. 1081–1096.

Deino, A., and Keith, J.D., 1997, Ages of volcanic and intrusive rocks in the Bingham mining district, Utah: Society of Economic Geologists Guidebook Series, v. 29, p. 91–100.

Denis, M., Pichavant, M., Poty, B., and Weisbrod, A., 1980, The Sierrita-Esperanza porphyry copper, Arizona, USA: Bulletin de Mineralogie, v. 103, p. 613–622.

Diamond, L.W., 1992, Stability of CO_2 clathrate hydrate + CO_2 liquid + CO_2 vapour + aqueous KCl-NaCl solutions—experimental-determination and application to salinity estimates of fluid inclusions: Geochimica et Cosmochimica Acta, v. 56, p. 273–280.

Dilles, H.J., 1987, Petrology of the Yerington batholith, Nevada: Evidence for evolution of porphyry copper ore fluids: Economic Geology, v. 82, p. 1750–1789.

Driesner, T., and Geiger, S., 2007, Numerical simulation of multiphase fluid flow in hydrothermal systems: Reviews in Mineralogy and Geochemistry, v. 65, p. 187–212.

Driesner, T., and Heinrich, C.A., 2007, The system H_2O-NaCl. Part I: Correlation formulae for phase relations in temperature-pressure-composition space from 0° to 1000°C, 0 to 5000 bars, and 0 to 1 X-NaCl: Geochimica et Cosmochimica Acta, v. 71, p. 4880–4901.

Eastoe, C.J., 1978, A fluid inclusion study of the Panguna porphyry copper deposit, Bougainville, Papua New Guinea: Economic Geology, v. 73, p. 721–748.

Etminan, H., 1977, Le porphyre cuprifere de Sar Cheshmeh (Iran): Role des phases fluides dans ales mecanismes d'alteration et de mineralisation: Unpublished Ph.D. thesis, Nancy, France, University of Nancy, 249 p.

Fournier, R.O., 1983, A method of calculating quartz solubilities in aqueous sodium-chloride solutions: Geochimica et Cosmochimica Acta, v. 47, p. 579–586.

Furrer, C., 2006, Fluid evolution and metal zonation at the Bingham porphyry Cu-Au-Mo deposit, Utah: Constraints from microthermometry and LA-ICPMS analysis of fluid inclusions: Unpublished M.Sc. thesis, Zurich, Switzerland, ETH Zurich, 96 p.

Gammons, C.H., and Williams-Jones, A.E., 1997, Chemical mobility of gold in the porphyry-epithermal environment: Economic Geology, v. 92, p. 45–59.

Gehrig, M., 1980, Phasengleichgewichte und PVT-Daten ternärer Mischungen aus Wasser, Kohledioxid und Natriumchlorid bis 3 kbar und 550°C: Unpublished Ph.D. thesis, Germany, University of Karlsruhe, 109 p.

Giggenbach, W.F., 1992, Magma degassing and mineral deposition in hydrothermal systems along convergent plate boundaries: Economic Geology, v. 87, p. 1927–1944.

Goldstein, R.H., and Reynolds, T.J., 1994, Systematics of fluid inclusions in diagenetic minerals: Society for Sedimentary Geology, 199 p.

Gruen, G., 2007, Distribution and orientation of veins in the Bingham Canyon porphyry Cu-Mo-Au deposit, Utah: Unpublished M.Sc. thesis, Zurich, Switzerland, ETH Zurich, 123 p.

Gruen, G., Heinrich, C.A., and Schroeder, K., 2010, The Bingham Canyon porphyry Cu-Mo-Au deposit. II. Vein geometry and ore shell formation by pressure-driven rock extension: Economic Geology, v. 105, p. 69–90.

Günther, D., Frischknecht, R., Heinrich, C.A., and Kahlert, H.J., 1997, Capabilities of an argon fluoride 193 nm excimer laser for laser ablation inductively coupled plasma mass spectrometry microanalysis of geological materials: Journal of Analytical Atomic Spectrometry, v. 12, p. 939–944.

Günther, D., Audétat, A., Frischknecht, R., and Heinrich, C.A., 1998, Quantitative analysis of major, minor and trace elements in fluid inclusions using laser ablation inductively coupled plasma mass spectrometry: Journal of Analytical Atomic Spectrometry, v. 13, p. 263–270.

Guillong, M., Latkoczy, C., Seo, J.H., Gunther, D., and Heinrich, C.A., 2008, Determination of sulfur in fluid inclusions by laser ablation ICP-MS: Journal of Analytical Atomic Spectrometry, v. 23, p. 1581–1589.

Hedenquist, J.W., and Lowenstern, J.B., 1994, The role of magmas in the formation of hydrothermal ore-deposits: Nature, v. 370, p. 519–527.

Heinrich, C.A., 2005, The physical and chemical evolution of low-salinity magmatic fluids at the porphyry to epithermal transition: A thermodynamic study: Mineralium Deposita, v. 39, p. 864–889.

Heinrich, C.A., Ryan, C.G., Mernagh, T.P., and Eadington, P.J., 1992, Segregation of ore metals between magmatic brine and vapor—a fluid inclusion study using PIXE microanalysis: Economic Geology, v. 87, p. 1566–1583.

Heinrich, C.A., Günther, D., Audétat, A., Ulrich, T., and Frischknecht, R., 1999, Metal fractionation between magmatic brine and vapor, determined by microanalysis of fluid inclusions: Geology, v. 27, p. 755–758.

Heinrich, C.A., Pettke, T., Halter, W.E., Aigner-Torres, M., Audétat, A., Gunther, D., Hattendorf, B., Bleiner, D., Guillong, M., and Horn, I., 2003, Quantitative multi-element analysis of minerals, fluid and melt inclusions by laser ablation-inductively coupled plasma-mass spectrometry: Geochimica et Cosmochimica Acta, v. 67, p. 3473–3497.

Heinrich, C.A., Driesner, T., Stefánsson, A., and Seward, T.M., 2004, Magmatic vapor contraction and the transport of gold from the porphyry environment to epithermal ore deposits: Geology, v. 32, p. 761–764.

Henley, R.W., and McNabb, A., 1978, Magmatic vapor plumes and groundwater interaction in porphyry copper emplacement: Economic Geology, v. 73, p. 1–20.

Inan, E.E., 2002, Occurrence of nukundamite at the Bingham porphyry Cu-Au-Mo district, Utah: Unpublished Ph.D. thesis, Stanford, CA, Stanford University, 221 p.

Irwin, J.J., and Roedder, E., 1995, Diverse origins of fluid in magmatic inclusions at Bingham (Utah, USA), Butte (Montana, USA), St-Austell (Cornwall, UK), and Ascension-Island (Mid-Atlantic, UK), indicated by laser microprobe analysis of Cl, K, Br, I, Ba Plus Te, U, Ar, Kr, and Xe: Geochimica et Cosmochimica Acta, v. 59, p. 295–312.

Kendrick, M.A., Burgess, R., Pattrick, R.A.D., and Turner, G., 2001a, Fluid inclusion noble gas and halogen evidence on the origin of Cu-porphyry mineralising fluids: Geochimica et Cosmochimica Acta, v. 65, p. 2651–2668.

——2001b, Halogen and Ar-Ar age determinations of inclusions within quartz veins from porphyry copper deposits using complementary noble gas extraction techniques: Chemical Geology, v. 177, p. 351–370.

Kennedy, G.C., 1950, A portion of the system silica-water: Economic Geology, v. 45, p. 629–653.

Kesler, S.E., Chryssoulis, S.L., and Simon, G., 2002, Gold in porphyry copper deposits: Its abundance and fate: Ore Geology Reviews, v. 21, p. 103–124.

Klemm, L.M., Pettke, T., Heinrich, C.A., and Campos, E., 2007, Hydrothermal evolution of the El Teniente deposit, Chile: Porphyry Cu-Mo ore deposition from low-salinity magmatic fluids: Economic Geology, v. 102, p. 1021–1045.

——2008, Fluid and source magma evolution of the Questa porphyry Mo deposit, New Mexico, USA: Mineralium Deposita, v. 43, p. 533–552.

Landtwing, M.R., 2004, Fluid evolution and ore mineral precipitation at the Bingham porphyry Cu-Au-Mo deposit, Utah, deduced from cathodoluminescence imaging and LA-ICPMS microanalysis of fluid inclusions: Unpublished Ph.D. thesis, Zurich, Switzerland, ETH Zurich, 260 p.

Landtwing, M.R., and Pettke, T., 2005, Relationships between SEM-cathodoluminescence response and trace-element composition of hydrothermal vein quartz: American Mineralogist, v. 90, p. 122–131.

Landtwing, M.R., Pettke, T., Halter, W.E., Heinrich, C.A., Redmond, P.B., Einaudi, M.T., and Kunze, K., 2005, Copper deposition during quartz dissolution by cooling magmatic-hydrothermal fluids: The Bingham porphyry: Earth and Planetary Science Letters, v. 235, p. 229–243.

Li, Y., Audétat, A., Lerchbaumer, L., and Xiong, X.L., 2009, Rapid Na, Cu exchange between synthetic fluid inclusions and external aqueous solutions: Evidence from LA-ICP-MS analysis: Geofluids, v. 9, p. 321–329.

Liebscher, A., 2007, Experimental studies in model fluid systems: Reviews in Mineralogy and Geochemistry, v. 65, p. 15–47.

Liebscher, A., and Heinrich, C.A., 2007, Fluid-fluid interactions in the earth's lithosphere: Fluid-Fluid Interactions, v. 65, p. 1–13.

Lindgren, W., 1905, The copper deposits of the Clifton-Morenci district, Arizona: U.S. Geological Survey Professional Paper 43, 375 p.

Lowenstern, J.B., Mahood, C.A., Rivers, M.L., and Sutton, S.R., 1991, Evidence for extreme partitioning of copper into a magmatic vapor phase: Science, v. 252, p. 1405–1409.

MacDonald, G.D., and Arnold, L.C., 1994, Geological and geochemical zoning of the Grasberg Igneous Complex, Irian-Jaya, Indonesia: Journal of Geochemical Exploration, v. 50, p. 143–178.

Murakami, H., Seo, J.H., and Heinrich, C.A., 2009, The relation between Cu/Au ratio and formation depth of porphyry-style Cu-Au ± Mo deposits: Mineralium Deposita, DOI10.1007/s00126–009–0255–1.

Nagaseki, H., and Hayashi, K.I., 2008, Experimental study of the behavior of copper and zinc in a boiling hydrothermal system: Geology, v. 36, p. 27–30.

Nash, J.T., 1976, Fluid-inclusion petrology: Data from porphyry copper deposits and applications to exploration: U.S. Geological Survey Professional Paper, 907 D, p. 1–16.

Pettke, T., Heinrich, C.A., Ciocan, A.C., and Günther, D., 2000, Quadrupole mass spectrometry and optical emission spectroscopy: Detection capabilities and representative sampling of short transient signals from laser-ablation: Journal of Analytical Atomic Spectrometry, v. 15, p. 1149–1155.

Pokrovski, G.S., Roux, J., and Harrichoury, J.C., 2005, Fluid density control on vapor-liquid partitioning of metals in hydrothermal systems: Geology, v. 33, p. 657–660.

Pokrovski, G.S., Borisova, A.Y., and Harrichoury, J.C., 2008, The effect of sulfur on vapor-liquid fractionation of metals in hydrothermal systems: Earth and Planetary Science Letters, v. 266, p. 345–362.

Pudack, C., Halter, W.E., Heinrich, C.A., and Pettke, T., 2009, Evolution of magmatic vapor to gold-rich epithermal liquid: The porphyry to epithermal transition at Nevados de Famatina, northwest Argentina: ECONOMIC GEOLOGY, v. 104, p. 449–477.

Redmond, P.B., 2002, Magmatic-hydrothermal fluids and copper-gold ore formation at Bingham Canyon, Utah: Unpublished Ph.D. thesis, Stanford, CA, Stanford University, 228 p.

Redmond, P.B., and Einaudi, M.T., 2010, The Bingham Canyon porphyry Cu-Mo-Au deposit. I. Sequence of intrusions, vein formation, and sulfide deposition: ECONOMIC GEOLOGY, v. 105, p. 43–68.

Redmond, P.B., Landtwing, M.R., and Einaudi, M.T., 2001, Cycles of porphyry dike emplacement, veining, alteration, and mineralisation in the Bingham porphyry Cu-Au-Mo deposit, Utah, *in* Piestrzyñski, A., et al., Mineral deposits at the beginning of the 21st century: Netherlands, A.A.Balkema, p. 473–476.

Redmond, P.B., Einaudi, M.T., Inan, E.E., Landtwing, M.R., and Heinrich, C.A., 2004, Copper deposition by fluid cooling in intrusion-centered systems: New insights from the Bingham porphyry ore deposit, Utah: Geology, v. 32, p. 217–220.

Roedder, E., 1971, Fluid inclusion studies on the porphyry-type ore deposits at Bingham, Utah, Butte, Montana, and Climax, Colorado: ECONOMIC GEOLOGY, v. 66, p. 98–120.

——1992, Fluid inclusion evidence for immiscibility in magmatic differentiation: Geochimica et Cosmochimica Acta, v. 56, p. 5–20.

Rusk, B.G., and Reed, M.H., 2002, Scanning electron microscope-cathodoluminescence analysis of quartz reveals complex growth histories in veins from the Butte porphyry copper deposit, Montana: Geology, v. 30, p. 727–730.

Rusk, B.G., Reed, M.H., Dilles, J.H., Klemm, L.M., and Heinrich, C.A., 2004, Compositions of magmatic hydrothermal fluids determined by LA-ICP-MS of fluid inclusions from the porphyry copper-molybdenum deposit at Butte, MT: Chemical Geology, v. 210, p. 173–199.

Rusk, B.G., Reed, M.H., and Dilles, J.H., 2008, Fluid inclusion evidence for magmatic-hydrothermal fluid evolution in the porphyry copper-molybdenum deposit at Butte, Montana: ECONOMIC GEOLOGY, v. 103, p. 307–334.

Sawkins, F.J., and Scherkenbach, D.A., 1981, High copper content of fluid inclusions in quartz from northern Sonora: Implications for ore-genesis theory: Geology, v. 9, p. 37–40.

Seedorff, E., Dilles, J.H., Proffett, J.M., Jr., Einaudi, M.T., Zurcher, L., Stavast, W.J.A., Johnson, D.A., and Barton, M.D., 2005, Porphyry deposits: Characteristics and origin of hypogene features: ECONOMIC GEOLOGY 100TH ANNIVERSARY VOLUME, p. 251–298.

Seo, J.H., Guillong, M., and Heinrich, C.A., 2009, The role of sulfur in the formation of magmatic-hydrothermal copper-gold deposits: Earth and Planetary Science Letters, in press.

Sillitoe, R.H., 1997, Characteristics and controls of the largest porphyry copper-gold and epithermal gold deposits in the circum-Pacific region: Australian Journal of Earth Sciences, v. 44, p. 373–388.

——2010, Porphyry copper systems: ECONOMIC GEOLOGY, v. 105, p. 3–41.

Sillitoe, R.H., and Bonham, H.F., 1990, Sediment-hosted gold deposits—distal products of magmatic-hydrothermal systems: Geology, v. 18, p. 157–161.

Simon, A.C., Pettke, T., Candela, P.A., Piccoli, P.M., and Heinrich, C.A., 2007, The partitioning behavior of As and Au in S-free and S-bearing magmatic assemblages: Geochimica et Cosmochimica Acta, v. 71, p. 1764–1782.

Simon, G., Kesler, S.E., Essene, E.J., and Chryssoulis, S.L., 2000, Gold in porphyry copper deposits: Experimental determination of the distribution of gold in the Cu-Fe-S system at 400° to 700°C: ECONOMIC GEOLOGY, v. 95, p. 259–270.

Stefánsson, A., and Seward, T.M., 2004, Gold(I) complexing in aqueous sulphide solutions to 500ºC at 500 bar: Geochimica et Cosmochimica Acta, v. 68, p. 4121–4143.

Steinberger, I., Driesner, T., Weis, P., and Heinrich, C.A., 2009, Towards a numerical reconstruction of the Bingham Canyon magmatic-hydrothermal ore system [abs.]: Geochimica et Cosmochimica Acta, v. 73, p. A1269.

Taylor, H.P.J., 1974, The application of oxygen and hydrogen isotope studies to problems of hydrothermal alteration and ore deposition: ECONOMIC GEOLOGY, v. 69, p. 843–883.

Ulrich, T., Günther, D., and Heinrich, C.A., 1999, Gold concentrations of magmatic brines and the metal budget of porphyry copper deposits: Nature, v. 399, p. 676–679.

——2002, The evolution of a porphyry Cu-Au deposit, based on LA-ICP-MS analysis of fluid inclusions: Bajo de la Alumbrera, Argentina (vol 96, pg 1743, 2001): ECONOMIC GEOLOGY, v. 97, p. 1888–1920.

Vanko, D.A., Bonnin-Mosbah, M., Philippot, P., Roedder, E., and Sutton, S.R., 2001, Fluid inclusions in quartz from oceanic hydrothermal specimens and the Bingham, Utah porphyry-Cu deposit: A study with PIXE and SXRF: Chemical Geology, v. 173, p. 227–238.

Vila, T., and Sillitoe, R.H., 1991, Gold-rich porphyry systems in the Maricunga belt, northern Chile: ECONOMIC GEOLOGY, v. 86, p. 1238–1260.

Waite, K.A., Keith, J.D., Christiansen, E.H., Whitney, J.A., Hattori, K.H., Tingey, D.G., and Hook, C.J., 1997, Petrogenesis of the volcanic and intrusive rocks associated with the Bingham Canyon porphyry Cu-Au-Mo deposit: Society of Economic Geologists Guidebook Series, v. 29, p. 69–90.

Weis, P., Driesner, T., Heinrich, C.A., Coumou, D., and Geiger, S., 2009, Flow of brine and vapour in subaerial and submarine magmatic hydrothermal systems: SGA Conference, Townsville, August 2009, Proceedings, p. 873–875.

Williams, T.J., Candela, P.A., and Piccoli, P.M., 1995, The partitioning of copper between silicate melts and two-phase aqueous fluids: An experimental investigation at 1 kbar, 800°C and 0.5 kbar, 850°C: Contributions to Mineralogy and Petrology, v. 121, p. 388–399.

Williams-Jones, A.E., and Heinrich, C.A., 2005, Vapor transport of metals and the formation of magmatic-hydrothermal ore deposits: ECONOMIC GEOLOGY, v. 100, p. 1287–1312.

Williams-Jones, A.E., Migdisov, A.A., Archibald, S.M., and Xiao, Z.F., 2002, Vapor-transport of ore metals: Gochemical Society Special Publication 7, p. 279–305.

Zajacz, Z., and Halter, W., 2009, Copper transport by high temperature, sulfur-rich magmatic vapor: Evidence from silicate melt and vapor inclusions in a basaltic andesite from the Villarrica volcano (Chile): Earth and Planetary Science Letters, v. 282, p. 115–121.

Zajacz, Z., Hanley, J.J., Heinrich, C.A., Halter, W.E., and Guillong, M., 2009, Diffusive reequilibration of quartz-hosted silicate melt and fluid inclusions: Are all metal concentrations unmodified? [ext. abs.]: ECROFI Meeting, 20th, University of Granada, Spain, September 2009, Extended Abstracts, p. 285–286.

Zezin, D., Migdisov, A.A., and Williams-Jones, A.E., 2008, The solubility of Au in H_2O-H_2S gas mixtures: Geochimica et Cosmochimica Acta, v. 72, p. A1076.